Spin Seebeck Imaging of Spin-Torque Switching in Antiferromagnetic Pt/NiO Heterostructures

Isaiah Gray,[1,2] Takahiro Moriyama,[3] Nikhil Sivadas,[1] Gregory M. Stiehl,[4] John T. Heron,[5] Ryan Need,[6] Brian J. Kirby,[6] David H. Low,[1] Katja C. Nowack,[4,2] Darrell G. Schlom,[7,2] Daniel C. Ralph,[4,2] Teruo Ono,[3] and Gregory D. Fuchs[1,2,*]

[1]*School of Applied and Engineering Physics, Cornell University, Ithaca, New York 14853, USA*
[2]*Kavli Institute for Nanoscale Science, Ithaca, New York 14853, USA*
[3]*Institute for Chemical Research, Kyoto University, Uji, Kyoto, 611-0011, Japan*
[4]*Department of Physics, Cornell University, Ithaca, New York 14853, USA*
[5]*Department of Materials Science and Engineering, University of Michigan, Ann Arbor, Michigan 48109, USA*
[6]*NIST Center for Neutron Research, National Institute of Standards and Technology, Gaithersburg, Maryland 20899, USA*
[7]*Department of Materials Science and Engineering, Cornell University, Ithaca, New York 14853, USA*

(Received 8 October 2018; revised manuscript received 9 August 2019; published 22 October 2019)

As electrical control of Néel order opens the door to reliable antiferromagnetic spintronic devices, understanding the microscopic mechanisms of antiferromagnetic switching is crucial. Spatially resolved studies are necessary to distinguish multiple nonuniform switching mechanisms; however, progress has been hindered by the lack of tabletop techniques to image the Néel order. We demonstrate spin Seebeck microscopy as a sensitive tabletop method for imaging antiferromagnetism in thin films and apply this technique to study spin-torque switching in Pt/NiO and Pt/NiO/Pt heterostructures. We establish the interfacial antiferromagnetic spin Seebeck effect in NiO as a probe of surface Néel order. By imaging before and after applying current-induced spin torque, we resolve spin domain rotation and domain wall motion. We correlate the changes in spin Seebeck images with electrical measurements of the average Néel orientation through the spin Hall magnetoresistance, confirming that we image antiferromagnetic order.

DOI: 10.1103/PhysRevX.9.041016

Subject Areas: Condensed Matter Physics, Spintronics

I. INTRODUCTION

Antiferromagnets (AFs), long relegated to a supporting role as the pinning layers in ferromagnetic spintronic devices [1,2], are emerging as the active element in antiferromagnetic spintronic devices [3–5]. In contrast to ferromagnets (FMs), AFs are insensitive to magnetic fields [6] and exhibit dynamics at the terahertz frequency scale [7,8]. Additionally, AFs have magnetotransport effects that enable electrical readout [9,10]. Taking advantage of these attractive properties, however, requires overcoming the challenge of reliably manipulating Néel order.

Recent breakthroughs in electrical [11,12] and optical [13,14] control provide a path toward reliable devices. In particular, electrical switching was demonstrated in the metals CuMnAs [11,15] and Mn_2Au [16] using Néel spin-orbit torque, in which the sign of the spin-orbit field from a dc current within the material alternates on each lattice site to coherently rotate the Néel vector [17]. Recently, electrical switching of an AF via spin torque was also demonstrated in insulating NiO [18–20] after several predictions [21,22]. In this mechanism, the dc current passing through an adjacent Pt layer generates a spin current through the spin Hall effect, which then exerts an antidamping torque on the spins at the Pt/NiO interface. Switching by antidamping spin torque does not require that the spin sublattices form inversion partners, which is required for Néel spin-orbit torque; hence, it is a more general approach that could enable all-electrical control over a wider variety of AFs.

Previous experiments have shown that AF switching is nonuniform [15,23,24] and heavily influenced by local magnetoelastic stresses [25]. Nominally identical samples display switching efficiency that varies by almost an order of magnitude at the same current density [18], demonstrating a need for better understanding the switching process at

*Corresponding author.
gdf9@cornell.edu

the domain level. Systematic spatially resolved studies are necessary to firmly establish the spin rotation mechanisms, the fraction of the domains that switch, and the reproducibility of switching.

A primary challenge when imaging antiferromagnetism is to find an experimental probe that is sensitive to Néel order and also provides the submicrometer resolution necessary to resolve domains. X-ray magnetic linear dichroism photoemission electron microscopy (XMLD-PEEM) has been the most reliable technique [23,26]; however, it requires a coherent x-ray source that is available at only a few facilities. Second-harmonic [27,28] and quadratic magneto-optical techniques [29,30] are available in a tabletop format, but the small signal sizes create a need for background subtraction, which can be a problem because antiferromagnets are difficult to fully saturate. Scanning-probe magnetometers are also available in tabletop format but require stray fields to be produced from the AF [31]. As an alternative, recent demonstrations of the AF anomalous Nernst effect [32] and AF spin Seebeck effect [33,34] open up the possibility of using spin-thermal effects as an imaging probe, because they can be directly sensitive to Néel order [3]. Previous work from both our group and others demonstrates high-sensitivity imaging of ferromagnetic order via the anomalous Nernst and longitudinal spin Seebeck effects [35–39], suggesting that a practical and sensitive magnetothermal microscope for Néel order can also be developed.

In this work, we use antiferromagnetic longitudinal spin Seebeck effect (AF LSSE) microscopy to image spin-orbit torque switching in Pt/NiO(111) bilayers and Pt/NiO(111)/Pt trilayers. We provide the first experimental demonstration of interfacial AF LSSE and use it as a direct probe of the Néel order to resolve 1–10-μm-size antiferromagnetic spin domains. By repeatedly imaging before and after spin-torque switching while varying the current density and direction in a variety of samples, we reveal effects of antidamping spin torque on the Néel order of NiO that would be difficult to establish either with device-level transport measurements or with limited beam time at an XMLD-PEEM facility. In particular, we show that switching occurs simultaneously by continuous rotation of the Néel orientation within AF domains and by current polarity-dependent AF domain wall motion.

The organization of this paper is as follows: We discuss the antiferromagnetic domain structure in NiO and present initial SSE images. We then establish the interfacial AF LSSE as the source of our signal, and we study spin-torque-induced domain rotation and domain wall motion.

II. IMAGING NÉEL ORDER WITH SPIN SEEBECK MICROSCOPY

A. Resolving antiferromagnetic domains in NiO

NiO is a collinear insulating antiferromagnet with a Néel temperature T_N of 523 K in the bulk [40]. Superexchange between Ni atoms along the $\langle 100 \rangle$ directions aligns the spins in ferromagnetic $\{111\}$ planes, in which spins on one plane are antiparallel to spins on the adjacent plane [26]. In the bulk, the AF domain structure is well known: Magnetostriction along $\langle 111 \rangle$ from the AF ordering causes crystallographic twinning, forming four T (twin) domains [41]. Within each T domain, dipolar next-nearest-neighbor coupling introduces a weak additional in-plane anisotropy along the three equivalent $[11\bar{2}]$ directions, forming three S (spin) domains per T domain [42,43]. In thin films, however, magnetoelastic stresses, the AF equivalent of the demagnetization field in FMs [25], introduce an additional effective anisotropy. This spatially inhomogeneous anisotropy pulls the spins out of well-defined $[11\bar{2}]$ directions, resulting in a disordered in-plane AF domain structure [44].

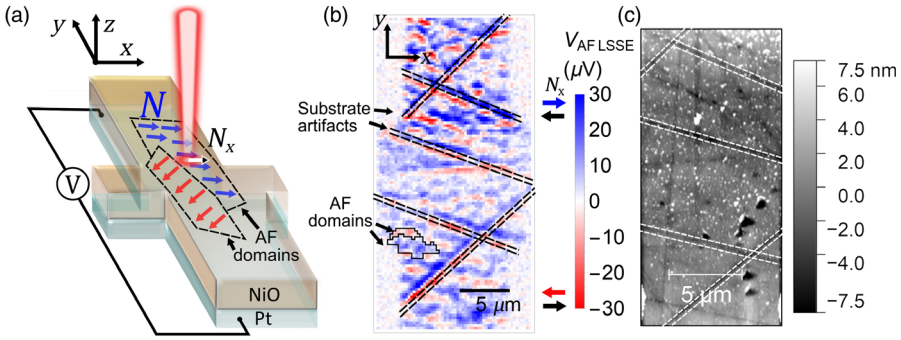

FIG. 1. Demonstration of AF LSSE microscopy. (a) Schematic of the measurement. A Ti:sapphire laser focused to 650 nm spot size thermally generates a local spin current $\boldsymbol{J}_s$ at the Pt/NiO interface, with spin polarization $\boldsymbol{\sigma}$ parallel to the local Néel orientation $\boldsymbol{N}$. The sign of $\boldsymbol{\sigma}$ is determined by the spin direction of the uncompensated monolayer. $\boldsymbol{J}_s$ is transduced into a charge current via the inverse spin Hall effect in the Pt, resulting in a voltage between the contacts. (b) AF LSSE image of a 10 μm × 50 μm Hall cross of MgO/5 nm Pt/7 nm NiO(111). Blue (red) contrast represents interfacial spins pointing right (left). Sharp straight lines highlighted by black dashed line are artifacts from the ordinary Seebeck effect, which may be due to scratches in the MgO substrate. (c) AFM height map of the same sample. Ordinary Seebeck artifacts in the AF LSSE image are accompanied by 1-nm-deep valleys in the height.

We resolve the spin domains in Pt/NiO bilayers and Pt/NiO/Pt trilayers with spin Seebeck effect microscopy [39] using a geometry illustrated in Fig. 1(a). We focus 3-ps-wide, 785 nm wavelength pulses from a Ti:sapphire laser down to a 650 nm spot size, which produces a local out-of-plane thermal gradient. We show in Supplemental Material [45] that the thermal gradient is dominated by an interfacial temperature drop ΔT at the Pt/NiO interfaces. In Sec. II B, we establish that ΔT generates a spin current $\boldsymbol{J}_s$ with polarization $\boldsymbol{\sigma}_{\text{int}}$ parallel to the orientation $\boldsymbol{s}_{\text{int}}$ of the closest monolayer of spins to the Pt interface. Within the Pt, the spin current is transduced into a charge current $\boldsymbol{J}_c \propto \boldsymbol{J}_s \times \boldsymbol{\sigma}_{\text{int}}$ via the inverse spin Hall effect (ISHE), which results in a voltage drop across the sample. By raster scanning the focused laser over the sample, we build a map of the ISHE voltage, which reports the in-plane component of $\boldsymbol{s}_{\text{int}}$ perpendicular to the voltage contacts.

An example AF LSSE image of an epitaxial MgO/5 nm Pt/7 nm NiO(111) device, deposited by sputtering and patterned into a 10 μm $\times$ 50 μm Hall cross by optical photolithography, is shown in Fig. 1(b). Blue and red contrast show interfacial spins pointing right and left, respectively. We acquire all images at room temperature and a zero magnetic field using 3.4 mJ/cm^2 laser fluence. By combining finite-element simulations of laser heating with electrical calibration using transient resistivity changes, we measure that this laser fluence locally heats the Pt and NiO layers to 360 and 330 K peak temperature, respectively, from the ambient temperature of 293 K. Note that the voltage we plot—denoted $V_{\text{AF LSSE}}$—is not the actual spin Seebeck voltage but rather a lock-in voltage after amplification, mixing, and normalization to account for impedance matching, which is also described in Supplemental Material [45].

Sharp straight lines in the AF LSSE image in Fig. 1(b), highlighted with black dashed lines, are also visible in the corresponding atomic force microscopy height map in Fig. 1(c) and may be due to polishing scratches in the MgO(111) substrate. Thermal discontinuities at these scratches cause artifacts in the AF LSSE signal from the ordinary Seebeck effect and are discussed further in Supplemental Material [45]. The rest of the contrast in the AF LSSE image in Fig. 1(b) represents antiferromagnetic spin domains: Examples are highlighted in black enclosures. Since the Pt is beneath the NiO in this sample and the voltage contacts are along y, in Fig. 1(b), we measure the N_x component of the bottom interfacial monolayer $\boldsymbol{s}_{\text{bottom}}$.

Currently, we cannot saturate the Néel vector along a given direction while imaging, which would require applying an *in situ* magnetic field greater than the spin-flop field (5 T in NiO [46]). Therefore, we cannot calibrate the AF LSSE voltage to an absolute Néel orientation. This limitation is an intrinsic difficulty of detecting antiferromagnetism and is also experienced by other imaging techniques, including XMLD-PEEM. Instead, the AF LSSE voltage represents the strength of the projection without absolute calibration. The size, shape, and distribution of AF domains are consistent with previous XMLD-PEEM imaging studies of thin-film NiO [44,47]. Note that only domains larger than the 650 nm laser spot size are resolved; some contrast in Fig. 1(b) extends down to the single-pixel limit and may represent incompletely resolved domains.

B. Evidence for interfacial antiferromagnetic LSSE

We attribute the signal in our images to an interfacial AF LSSE. Although the ferromagnetic LSSE is well established both in the bulk [48–50] and at the interface [51–53], the AF LSSE was initially predicted not to exist for a collinear AF [54] and was only recently observed [33,34]. In a collinear AF, the two spin sublattices produce two degenerate magnon modes [55], which produce spin current in opposite directions under a thermal gradient. Therefore, unless the degeneracy is lifted, there is no net spin current [54]. The degeneracy can be lifted in the AF bulk by applying a large magnetic field [33,34] or by exploiting anisotropies that result in additional magnon modes [56,57]. The degeneracy can also be lifted by inversion symmetry breaking at the interface, resulting in an interfacial AF LSSE that has been predicted [58] but has not been previously reported.

The mechanism of the interfacial AF LSSE is schematically illustrated in Figs. 2(a) and 2(b). AF interfaces can be *uncompensated* as in Fig. 2(a), meaning the layer closest to the surface contains an excess of one sublattice, or *compensated* as in Fig. 2(b), in which adjacent spins are antiparallel in each growth plane. In the uncompensated case, an interfacial temperature difference ΔT across the surface normal $\hat{\boldsymbol{n}}$ induces a local spin current $\boldsymbol{J}_s \| \Delta T \hat{\boldsymbol{n}}$ whose polarization effectively alternates in sign at each monolayer, following the local spin polarization. The layer closest to the Pt interface—$\boldsymbol{s}_{\text{int}}$—is more strongly exchange coupled to the spins in the Pt layer than the other layers are [59], and, therefore, a net spin current $\boldsymbol{J}_s$ diffuses into the Pt with polarization $\boldsymbol{\sigma} \| \boldsymbol{s}_{\text{int}}$ [58]. Note that $\boldsymbol{s}_{\text{int}}$ is $\boldsymbol{s}_{\text{top}}$ if the Pt is above the NiO and $\boldsymbol{s}_{\text{bottom}}$ if the Pt is beneath the NiO.

At the compensated interface, illustrated in Fig. 2(b), the symmetry between magnon modes is preserved. Therefore, the spin current produced by ΔT is zero on every $\langle 111 \rangle$ plane as long as the in-plane spatial extent of ΔT (650 nm for the laser spot) is much greater than the in-plane lattice spacing [0.4 nm in NiO(001)]. Although the uncompensated interface in the schematic in Fig. 2(a) is atomically flat, the presence of roughness in real samples does not alter the interpretation of the AF LSSE signal as long as the lateral length scale of average height variation is also much smaller than the laser spot diameter (see Supplemental Material [45] for more details).

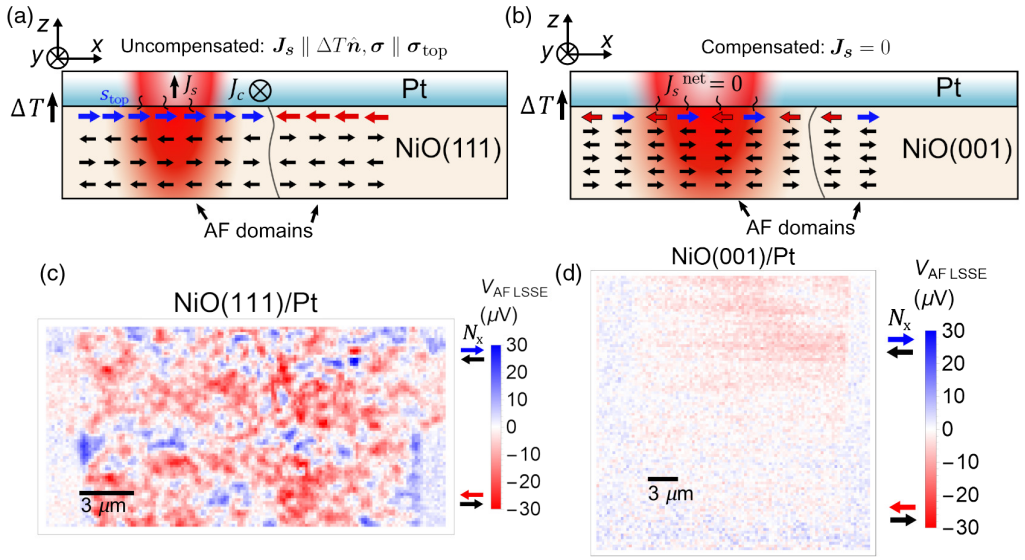

FIG. 2. Mechanism of the interfacial AF LSSE. (a) Schematic illustrating the interfacial AF LSSE at an uncompensated interface. A thermal gradient produces spin current $\boldsymbol{J}_s$ with polarization $\boldsymbol{\sigma}$ parallel to the spin orientation of the interfacial uncompensated monolayer ($\boldsymbol{s}_{top}$ in the diagram). (b) Schematic illustrating the lack of AF LSSE at a compensated interface. The net spin current produced by every monolayer is zero. (c),(d) AF LSSE images of uncompensated $MgAl_2O_4$ (111)/165 nm NiO(111)/6 nm Pt and compensated MgO(001)/136 nm NiO(001)/6 nm Pt, respectively. The lack of $V_{AF\ LSSE}$ signal from NiO(001) compared to NiO(111) indicates that $V_{AF\ LSSE}$ originates from the uncompensated interface.

Our experimental test of interfacial AF LSSE is shown in Figs. 2(c) and 2(d). We take AF LSSE images of MBE-grown $MgAl_2O_4$/165 nm NiO(111)/Pt and MgO(001)/136 nm NiO(001)/Pt, which have uncompensated and compensated interfaces, respectively. Both samples are patterned into 20-μm-wide Hall bars with similar growth conditions, sample resistivities, and interface qualities as shown in Supplemental Material [45]. Since the Pt is above the NiO, we measure $\boldsymbol{s}_{top}$ here. We find that AF LSSE images of NiO(001) yield an order of magnitude lower voltage compared with NiO(111). The residual contrast in NiO(001) images is nearly uniform and does not resemble domains; it may be due to capacitive coupling or other small experimental artifacts. Although the preferred spin orientation in MgO(001)/NiO(001) is not well established [19,20], recent XMLD-PEEM and magneto-optical images of 10-nm-thick NiO(001) on MgO(001) indicate approximately 10° out-of-plane tilt [30], which would reduce $V_{AF\ LSSE}$ by 2%. If the spins in our 136-nm-thick NiO(001) are relaxed to the bulk orientation, they would point 35° out of plane (the angle between $\{11\bar{2}\}$ and $\{001\}$). This result would reduce $V_{AF\ LSSE}$ by 20%, which is still not enough to account for the order-of-magnitude difference. Therefore, our results are consistent with a model of an uncompensated interface. Our results also indicate that bulk AF LSSE [56,60] does not significantly contribute to our signal. This interpretation is further supported by finite-element simulations, discussed in Supplemental Material [45], which show that the laser-induced thermal profile is dominated by temperature drops at the Pt/NiO interfaces rather than a temperature gradient in the NiO bulk.

We can further distinguish between an AF LSSE at an uncompensated interface and a possible FM LSSE originating from pinned uncompensated moments (UMs) [61]. These UMs could arise from interfacial roughness [62] or defects, both at the interface and in the bulk of the AF [63], and would be detectable by other magnetometry techniques. Therefore, we perform scanning SQUID microscopy at 4 K to search for microscopic moments and polarized neutron reflectometry at room temperature to detect a global moment at 1 T applied field. Both sets of measurements are made on sputtered samples and are described in more detail in Supplemental Material [45]. We find no magnetic moment within sensitivity, which places an upper limit of $8 \times 10^{-4}\mu_B$/Ni on the local moment that could be present. From this value, we calculate a maximum bulk magnetization of 110 A/m in our NiO, 3 orders of magnitude less than the bulk magnetization in YIG at room temperature. Based on these measurements, we rule out a FM LSSE and conclude that the AF LSSE signal in NiO arises from the uncompensated interface.

III. IMAGING SPIN-TORQUE SWITCHING IN Pt/NiO/Pt TRILAYERS

Having established a mechanism for the signal contrast, we move onto image current-induced spin-torque switching in Hall crosses, initially following the procedure in Refs. [18,19]. We apply a dc writing current and characterize the Néel state electrically, using the antiferromagnetic analog of spin Hall magnetoresistance (SMR)

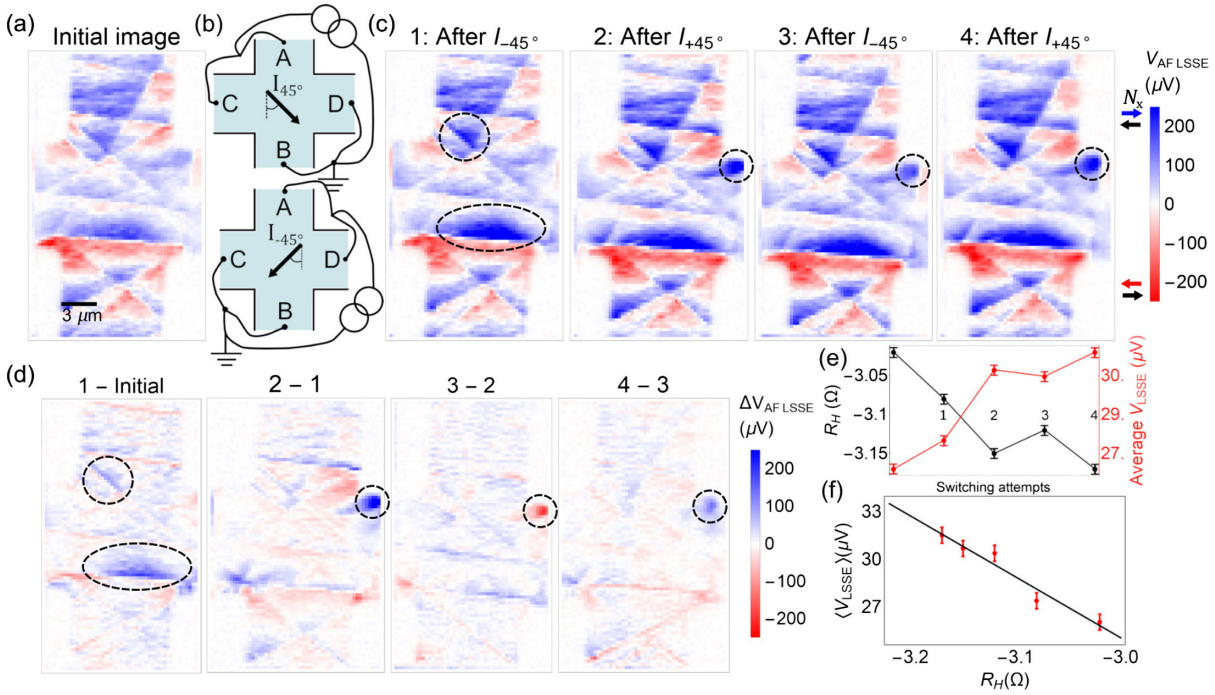

FIG. 3. AF LSSE imaging of spin-torque switching in a 5 nm Pt/13 nm NiO(111)/5 nm Pt trilayer. (a) The initial image, taken before applying the current. (b) Schematic of the writing process. We apply a current to two arms of the Hall cross such that the current density in the center flows along 45° diagonals. (c) Imaging while toggling between $I_{45°}$ and $I_{-45°}$. Highlighted in dashed lines are changes in contrast at the top right corner, where the current density is greatest, and near apparent substrate scratches, where the spins may be less strongly exchange coupled. (d) Successive differences between the AF LSSE images in (a), showing the domains that switch more clearly. Both positive and negative contrast in difference images may reflect domains rotating in opposite directions. (e) R_H and the integrated AF LSSE signal $\langle V_{\mathrm{AF\ LSSE}}\rangle$, measured while toggling between $I_{45°}$ and $I_{-45°}$. Values corresponding to the images shown are labeled. (f) $\langle V_{\mathrm{AF\ LSSE}}\rangle$ plotted as a function of SMR, measured through changes in the Hall resistance R_H. The near-linear correlation shows the small-angle correspondence between $\langle V_{\mathrm{AF\ LSSE}}\rangle$ and R_H.

[64–66] by measuring the change in the Hall resistance R_H: $R_H = -\Delta R_{\mathrm{SMR}} \sin\theta\cos\theta$, where θ is the angle between the spatially averaged Néel vector $\boldsymbol{N}$ and the reading current $\boldsymbol{J}_R$. To maximize ΔR_H, we apply a writing current to two of the arms of the Hall cross such that the current density in the center of the device flows along ±45° [schematically illustrated in Fig. 3(b)]. Using a finite-element simulation described further in Supplemental Material [45], we estimate a writing current density of 8.0×10^7 A/cm^2 at the corners and 3.1×10^7 A/cm^2 in the center of the cross. Hereafter, we refer only to the density in the center of the cross, J_W. After each application of writing current, we measure the Hall resistance R_H by applying a reading current density $J_R = 1.5 \times 10^6$ A/cm^2 from A to B and measuring the voltage from C to D in Fig. 3(b).

We initially employ epitaxial sputtered 5 nm Pt/13 nm NiO(111)/5 nm Pt trilayers, following the argument of Ref. [18] (further demonstrated in Ref. [67] in synthetic antiferromagnets) that spin torque at both the top and bottom interfaces of the NiO leads to more coherent rotation of the Néel orientation throughout the AF thickness. There is a potential complication interpreting the AF LSSE images in trilayers, because both Pt/NiO interfaces can contribute to the signal; however, we show in Supplemental Material [45] that the presence of two simultaneously contributing interfaces does not alter the interpretation of $V_{\mathrm{AF\ LSSE}}$ as long as the AF domains are continuous in thickness, which we expect for our trilayer samples. The AF domains in the trilayer are substantially larger (5–10 μm) than the domains in the bilayer in Fig. 1 (submicrometer to 2 μm), which most likely is due to differing growth conditions but which requires further study.

AF LSSE images of a trilayer before and after four sequential applications of $J_W = 3.1 \times 10^7$ A/cm^2 are shown in Figs. 3(a) and 3(c), with the writing current direction alternating between +45° and −45°. Although most domains are unaltered, we observe changes in contrast (highlighted inside the black dashed enclosures) at a sample corner, where the current density is highest, and near apparent substrate scratches, where the spins may be less strongly exchange coupled. To quantify these changes to the Néel orientation, we calculate sequential differences between images, shown in Fig. 3(d). We observe both positive and negative changes in contrast in different parts of the sample, which could be due to different AF domains

rotating in opposite directions, as seen in imaging studies of switching in CuMnAs [23]. At the current density used, we estimate that the maximum Oersted field is approximately 10 mT. We show in Supplemental Material [45] that the AF LSSE signal is unaffected by field up to ±250 mT, which rules out the Oersted field from the writing current as the mechanism responsible for switching.

To compare AF LSSE imaging with electrical measurements of Néel order using R_H, we take the average of all the pixels in and near the cross center in each image (described in Supplemental Material [45]) to obtain the integrated AF LSSE signal $\langle V_{\mathrm{AF\,LSSE}}\rangle$. Although $\langle V_{\mathrm{AF\,LSSE}}\rangle$ and R_H are both measures of the average Néel orientation in the cross center, they have different symmetries: $R_H \propto \cos\theta \sin\theta$, where θ is the angle between the average Néel vector and the SMR reading current $\boldsymbol{J}_R$, while $\langle V_{\mathrm{AF\,LSSE}}\rangle \propto \cos\phi$, where ϕ is the angle between the average Néel vector and the voltage contacts. Since we apply $\boldsymbol{J}_R$ along x in this device, here $\theta = \phi - \pi/2$ and $\langle V_{\mathrm{AF\,LSSE}}\rangle \propto -\sin\theta$. In this sample, most of the changes in contrast occur where $\boldsymbol{N}$ appears to be nearly saturated in the $+x$ direction, so that locally $\theta \approx 0$. Near $\theta = 0$, $\sin\theta\cos\theta \approx \sin\theta$. Therefore, $\langle V_{\mathrm{AF\,LSSE}}\rangle$ tracks R_H point by point, shown in Fig. 3(e). Plotting one versus the other yields a near-linear correlation with a negative slope, shown in Fig. 3(f) with a linear fit drawn as a guide to the eye. This correspondence indicates that changes in contrast indeed represent antiferromagnetic switching.

We expect that AF switching can occur either by domain rotation, which would manifest in the AF LSSE images as changes of contrast level within domains, or by domain wall motion. The switching in Fig. 3 manifests as changes in contrast within domains while domain walls remain stationary within the resolution limit, which indicates domain rotation. In this sample, we observe changes in color shade but not changes in sign of N_x (blue to red or vice versa), which indicates that N rotates by acute angles. Although we cannot obtain an absolute angle of rotation, we can obtain a lower bound by taking the maximum and minimum $V_{\mathrm{AF\,LSSE}}$ to correspond to $\theta = 90°$ and $-90°$, respectively. In this case, we estimate that the average Néel vector at the corner rotates 22° between images 1 and 2 in Fig. 3(c) and 10° between images 2 and 3.

Previous studies of magnetic-field-induced domain rotation in 120-nm-thick NiO [66] model switching as 120° flopping between $\langle 11\bar{2}\rangle$ in-plane easy axes. In our samples, however, the domains have random in-plane orientation, which is consistent with XMLD-PEEM images of similar Pt/NiO/Pt trilayers [18]. This domain configuration is consistent with an increased role of magnetoelastic stress in our 6-nm-thick samples, which favors a multidomain state with zero average strain. While the effective field from in-plane anisotropy is $H_{Az} = 11$ mT in bulk NiO [57], the destressing field reported in 120-nm-thick NiO in Ref. [66] is 46 mT. We expect the destressing field to be even higher in 6 nm NiO. Therefore, because the spins are not restricted to the $\langle 11\bar{2}\rangle$ axes in our samples, they can switch by continuous in-plane rotation.

IV. RESOLVING DOMAIN ROTATION AND DOMAIN WALL MOTION IN MgO/Pt/NiO BILAYERS

After correlating the AF LSSE images with an electrical readout of the Néel order through SMR in Pt/NiO/Pt trilayers, we move on to imaging switching in the sputtered NiO(111)/Pt bilayer from Fig. 1 after applying a current along the device channel. The bilayer does not have the potential difficulty of superposing signal from two Pt/NiO interfaces. Furthermore, applying a current along the device channel yields more uniform current density, leading to larger-scale, more easily resolvable changes in image contrast. Figure 4(a) shows AF LSSE images before switching and then after applying progressively greater current densities, from 5.0×10^7 A/cm^2 at 20 mA to 1.1×10^8 A/cm^2 at 42 mA, first at positive polarity (flowing down) and then negative polarity (flowing up). Prominent regions of switching are highlighted in the black enclosure as a guide to the eye.

Because the switching in Fig. 4 is spatially distributed and nonuniform, and AF LSSE and SMR have different symmetries, we cannot correlate the AF LSSE signal with SMR like we do in Fig. 3. Therefore, we compare our AF LSSE images to theoretical models of switching. References [18,19] model switching in the high-current limit as coherent rotation of spins within an AF domain (domain rotation), which we observe in Fig. 3. The model in Ref. [20] distinguishes three separate switching mechanisms, with predictions summarized as follows.

(1) The out-of-plane component of the spin current rotates spins within the easy plane, rotating all AF domains by the same angle.
(2) The in-plane component of the spin torque creates an additional effective anisotropy, resulting in a translational ponderomotive force $\boldsymbol{F}_{\mathrm{pond}}$ proportional to J_W^2 on the AF domain wall. $\boldsymbol{F}_{\mathrm{pond}}$ rotates $\boldsymbol{N} \| \boldsymbol{J}_W$ and is current polarity independent.
(3) The spin torque directly rotates the spins within the domain walls, leading to a chiral domain wall force $\boldsymbol{F}_{\mathrm{DW}}$ that goes as $\boldsymbol{J}_W$. $\boldsymbol{F}_{\mathrm{DW}}$ can rotate $\boldsymbol{N}$ either towards or perpendicular to $\boldsymbol{J}_W$, depending on the domain wall chirality; therefore, it should have no net effect on R_H with randomly oriented domains. $\boldsymbol{F}_{\mathrm{DW}}$ should also reverse direction when $\boldsymbol{J}_W$ reverses.

To quantitatively characterize the switching, we take sequential image differences in Fig. 4(b). Cumulative difference images as well as AF LSSE images after +20 and −42 mA are given in Supplemental Material [45]. After applying 30 mA, as seen in image 2–1, we see large-scale, nearly uniform positive (blue) contrast in the lower

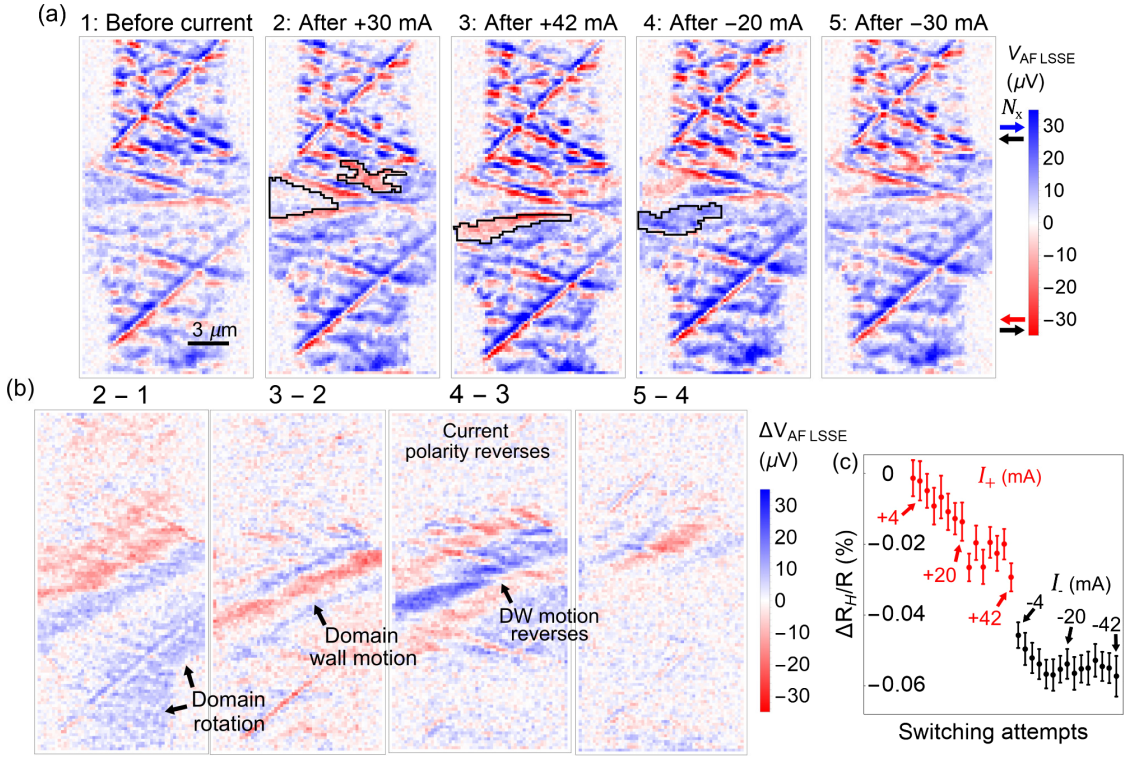

FIG. 4. Switching in the Pt/NiO bilayer from Fig. 1 after applying a current along the channel direction. (a) AF LSSE images before and after applying current. We apply first a positive current, flowing down, and then a negative current, flowing up. Some prominent regions of switching are highlighted in the black line, including domain growth after +42 mA and domain wall motion after −20 mA. (b) Sequential differences from the initial state (1). Large-scale patterns of nearly uniform positive contrast in the lower portion of 2–1 show different AF domains rotating by the same angle. We observe domain wall motion after +42 mA that reverses direction when the current polarity is reversed, consistent with theoretical predictions of a chiral domain wall force $\boldsymbol{F}_{\mathrm{DW}}$. (c) SMR measurements of the average Néel orientation for a similar Pt/NiO bilayer after applying the same currents, first positive and then negative (labeled in mA). R_H does not depend on current polarity, which is consistent with domain wall motion due to $\boldsymbol{F}_{\mathrm{DW}}$.

half of the cross, labeled *domain rotation*. More uniform contrast in the difference images than in the AF LSSE images themselves indicates that different AF domains are rotating by the same angle, consistent with the out-of-plane spin torque in mechanism 1 in Ref. [20]. This domain rotation saturates after +30 mA (7.5×10^7 A/cm^2) and does not reverse when the current polarity reverses. We primarily observe $|N_x|$ increasing—blue domains become more blue and red domains more red—which means $\boldsymbol{N}$ rotates $\perp \boldsymbol{J}_W$.

From images 2 and 3 in the AF LSSE images in Fig. 4(a), we resolve switching by domain wall motion, which appears as a negative (red) horizontal stripe in the sequential 3–2 image in Fig. 4(b). Domain rotation and domain wall motion occur in response to a writing current as low as 4 mA (1.0×10^7 A/cm^2). Interestingly, we find that the domains continue to move for 2–3 hr after the current is turned off (shown in Supplemental Material [45]), which may be due to magnetoelastic stresses causing subthreshold domain wall creep after the spin torque rotates the domains out of equilibrium. Although the domain configuration after +42 mA in 3 does not creep in time, the domain wall motion reverses after applying −20 mA, seen in 4–3, and subsequently almost ceases, seen by weaker contrast in 5–4 after applying −30 mA. DW motion that reverses when the current polarity is reversed points to the chiral force $\boldsymbol{F}_{\mathrm{DW}}$ as the origin. In Fig. 4(c), we show SMR measurements of a similar MgO/Pt/NiO cross while applying the same currents, first positive and then negative. We find that R_H does not depend on current polarity, which is consistent with the prediction that the effects of $\boldsymbol{F}_{\mathrm{DW}}$ would not be reflected by changes in R_H.

Summarizing our results, we identify both domain rotation and domain wall motion acting simultaneously, which are consistent with the out-of-plane spin torque and chiral domain force, respectively, described in Ref. [20]. At the current densities applied, from 1.0×10^7 to 1.0×10^8 A/cm^2, we do not observe $\boldsymbol{N}$ rotating towards $\boldsymbol{J}_W$ from the ponderomotive force $\boldsymbol{F}_{\mathrm{pond}}$, which is expected to dominate at higher current densities (above 7–9×10^7 A/cm^2, depending on the strain). Further imaging studies on thicker NiO samples with less strain may be required to observe $\mathbf{F}_{\mathrm{pond}}$.

Our results complement the XMLD-PEEM images of switching in Refs. [18,20]. Although Ref. [18] shows domain wall motion and Ref. [20] appears to show domain rotation in response to current, distinguishing several simultaneously acting switching mechanisms requires systematic repeated imaging of multiple samples, which may not be practical with the limited beam time at a synchrotron facility.

V. CONCLUSION

In conclusion, we demonstrate interfacial AF LSSE as the basis for a powerful tabletop technique for imaging in-plane Néel order in an AF insulator. This magnetothermal microscope uses equipment that is readily available in many laboratories, thus enabling in-depth and high-throughput studies of AF spintronics, which was previously limited by the availability of a few coherent x-ray facilities. Using this capability, we probe the microscopic behavior of spin-torque switching of Néel order in Pt/NiO/Pt trilayers and Pt/NiO bilayers. We find that switching occurs by domain rotation and domain wall motion acting simultaneously and that magnetoelastic stresses play an important role in determining both the equilibrium domain structure and the fraction of domains that switch. These insights provide critical understanding of spin-torque switching in NiO and point the way towards systematic optimization of antiferromagnetic spintronic devices. Moreover, we expect AF LSSE microscopy to extend to a wide variety of antiferromagnetic insulators with uncompensated interfaces, which can aid in the development of new device technologies based on different antiferromagnets.

ACKNOWLEDGMENTS

We thank Rembert Duine, Yaroslav Tserkovnyak, Jason Bartell, Emrah Turgut, and Farhan Rana for useful discussions. This research was supported by the Cornell Center for Materials Research with funding from the NSF MRSEC program (DMR-1719875) and by JSPS KAKENHI Grants No. JP15H05702, No. JP17H04924, and No. JP17H05181. This work made use of the CCMR Shared Facilities and the Cornell NanoScale Facility, an NNCI member supported by NSF Grant No. NNCI-1542081. N. S. acknowledges National Science Foundation [Platform for the Accelerated Realization, Analysis, and Discovery of Interface Materials (PARADIM)] under Cooperative Agreement No. DMR-1539918 and Cornell University Center for Advanced Computing for his time at Cornell University.

[1] B. Dieny, V. S. Speriosu, S. S. P. Parkin, B. A. Gurney, D. R. Wilhoit, and D. Mauri, *Giant Magnetoresistive in Soft Ferromagnetic Multilayers*, Phys. Rev. B **43**, 1297 (1991).

[2] H. N. Fuke, K. Saito, Y. Kamiguchi, H. Iwasaki, and M. Sahashi, *Spin-Valve Giant Magnetoresistive Films with Antiferromagnetic Ir-Mn Layers*, J. Appl. Phys. **81**, 4004 (1997).

[3] V. Baltz, A. Manchon, M. Tsoi, T. Moriyama, T. Ono, and Y. Tserkovnyak, *Antiferromagnetic Spintronics*, Rev. Mod. Phys. **90**, 015005 (2018).

[4] T. Jungwirth, X. Marti, P. Wadley, and J. Wunderlich, *Antiferromagnetic Spintronics*, Nat. Nanotechnol. **11**, 231 (2016).

[5] J. Železný, P. Wadley, K. Olejník, A. Hoffman, and H. Ohno, *Spin Transport and Spin Torque in Antiferromagnetic Devices*, Nat. Phys. **14**, 220 (2018).

[6] A. N. Bogdanov, A. V. Zhuravlev, and U. K. Rößler, *Spin-Flop Transition in Uniaxial Antiferromagnets: Magnetic Phases, Reorientation Effects, and Multidomain States*, Phys. Rev. B **75**, 094425 (2007).

[7] K. Olejník, T. Seifert, Z. Kašpar, V. Novák, P. Wadley, R. P. Campion, M. Baumgartner, P. Gambardella, P. Němec, J. Wunderlich, J. Sinova, P. Kužel, M. Müller, T. Kampfrath, and T. Jungwirth, *Terahertz Electrical Writing Speed in an Antiferromagnetic Memory*, Sci. Adv. **4**, eaar3566 (2018).

[8] P. Bowlan, S. A. Trugman, D. A. Yarotski, A. J. Taylor, and R. P. Prasankumar, *Using Ultrashort Terahertz Pulses to Directly Probe Spin Dynamics in Insulating Antiferromagnets*, J. Phys. D **51**, 194003 (2018).

[9] I. Fina, X. Marti, D. Yi, J. Liu, J. H. Chu, C. Rayan-Serrao, S. Suresha, A. B. Shick, J. Železný, T. Jungwirth, J. Fontcuberta, and R. Ramesh, *Anisotropic Magnetoresistance in an Antiferromagnetic Semiconductor*, Nat. Commun. **5**, 4671 (2014).

[10] X. Marti, I. Fina, C. Frontera, J. Liu, P. Wadley, Q. He, R. J. Paull, J. D. Clarkson, J. Kudrnoský, I. Turek, J. Kuneš, D. Yi, J.-H. Chu, C. T. Nelson, L. You, E. Arenholz, S. Salahuddin, J. Fontcuberta, T. Jungwirth, and R. Ramesh, *Room-Temperature Antiferromagnetic Memory Resistor*, Nat. Mater. **13**, 367 (2014).

[11] P. Wadley *et al.*, *Electrical Switching of an Antiferromagnet*, Science **351**, 587 (2016).

[12] K. Olejník, V. Schuler, X. Marti, V. Novák, Z. Kašpar, P. Wadley, R. P. Campion, K. W. Edmonds, B. L. Gallagher, J. Garces, M. Baumgartner, P. Gambardella, and T. Jungwirth, *Antiferromagnetic CuMnAs Multi-Level Memory Cell with Microelectronic Compatibility*, Nat. Commun. **8**, 15434 (2017).

[13] T. Higuchi and M. Kuwata-Gonokami, *Control of Antiferromagnetic Domain Distribution via Polarization-Dependent Optical Annealing*, Nat. Commun. **7**, 10720 (2016).

[14] S. Manz, M. Matsubara, T. Lottermoser, J. Buchi, A. Iyama, T. Kimura, D. Meier, and M. Fiebig, *Reversible Optical Switching of Antiferromagnetism in* $TbMnO_3$, Nat. Photonics **10**, 653 (2016).

[15] P. Wadley, S. Reimers, M. Grzybowski, C. Andrews, M. Wang, J. S. Chauhan, B. L. Gallagher, R. P. Campion, K. W. Edmonds, S. S. Dhesi, F. Maccherozzi, V. Novak, J. Wunderlich, and T. Jungwirth, *Current Polarity-Dependent Manipulation of Antiferromagnetic Domains*, Nat. Nanotechnol. **13**, 362 (2018).

[16] S. Y. Bodnar, L. Smejkal, I. Turek, T. Jungwirth, O. Gomonay, J. Sinova, A. A. Sapozhnik, H. J. Elmers,

M. Klaui, and M. Jourdan, *Writing and Reading Antiferromagnetic* Mn_2Au *by Néel Spin-Orbit Torques and Large Anisotropic Magnetoresistance*, Nat. Commun. **9**, 348 (2018).

[17] J. Železný, H. Gao, K. Výborný, J. Zemen, J. Mašek, A. Manchon, J. Wunderlich, J. Sinova, and T. Jungwirth, *Relativistic Néel-Order Fields Induced by Electrical Current in Antiferromagnets*, Phys. Rev. Lett. **113**, 157201 (2014).

[18] T. Moriyama, K. Oda, T. Ohkochi, M. Kimata, and T. Ono, *Spin Torque Control of Antiferromagnetic Moments in NiO*, Sci. Rep. **8**, 14167 (2018).

[19] X. Z. Chen, R. Zarzuela, J. Zhang, C. Song, X. F. Zhou, G. Y. Shi, F. Li, H. A. Zhou, W. J. Jiang, F. Pan, and Y. Tserkovnyak, *Antidamping-Torque-Induced Switching in Biaxial Antiferromagnetic Insulators*, Phys. Rev. Lett. **120**, 207204 (2018).

[20] L. Baldrati, O. Gomonay, A. Ross, M. Filianina, R. Lebrun, R. Ramos, C. Leveille, T. Forrest, F. Maccherozzi, E. Saitoh, J. Sinova, and M. Kläui, *Mechanism of Néel Order Switching in Antiferromagnetic Thin Films Revealed by Magnetotransport and Direct Imaging*, arXiv:1810.11326.

[21] R. Cheng, J. Xiao, Q. Niu, and A. Brataas, *Spin Pumping and Spin-Transfer Torques in Antiferromagnets*, Phys. Rev. Lett. **113**, 057601 (2014).

[22] P. M. Haney and A. H. MacDonald, *Current-Induced Torques due to Compensated Antiferromagnets*, Phys. Rev. Lett. **100**, 196801 (2008).

[23] M. J. Grzybowski, P. Wadley, K. W. Edmonds, R. Beardsley, V. Hills, R. P. Campion, B. L. Gallagher, J. S. Chauhan, V. Novak, T. Jungwirth, F. Maccherozzi, and S. S. Dhesi, *Imaging Current-Induced Switching of Antiferromagnetic Domains in CuMnAs*, Phys. Rev. Lett. **118**, 057701 (2017).

[24] A. A. Sapozhnik, M. Filianina, S. Yu. Bodnar, A. Lamirand, M.-A. Mawass, Y. Skourski, H.-J. Elmers, H. Zabel, M. Kläui, and M. Jourdan, *Direct Imaging of Antiferromagnetic Domains in* Mn_2Au *Manipulated by High Magnetic Fields*, Phys. Rev. B **97**, 134429 (2018).

[25] H. Gomonay and V. M. Loktev, *Magnetostriction and Magnetoelastic Domains in Antiferromagnets*, J. Phys. Condens. Matter **14**, 3959 (2002).

[26] F. U. Hillebrecht, H. Ohldag, N. B. Weber, C. Bethke, U. Mick, M. Weiss, and J. Bahrdt, *Magnetic Moments at the Surface of Antiferromagnetic NiO(100)*, Phys. Rev. Lett. **86**, 3419 (2001).

[27] M. Nývlt, F. Bisio, and J. Kirschner, *Second Harmonic Generation Study of the Antiferromagnetic NiO(001) Surface*, Phys. Rev. B **77**, 014435 (2008).

[28] J.-Y. Chauleau, E. Haltz, C. Arrétéro, S. Fusil, and M. Viret, *Multi-Stimuli Manipulation of Antiferromagnetic Domains Assessed by Second-Harmonic Imaging*, Nat. Mater. **16**, 803 (2017).

[29] T. Higo, H. Man, D. B. Gopman, L. Wu, T. Koretsune, O. M. J. van't Erve, Y. P. Kabanov, D. Rees, Y. Li, M.-T. Suzuki, S. Patankar, M. Ikhlas, C. L. Chien, R. Arita, R. D. Shull, J. Orenstein, and S. Nakatsuji, *Large Magneto-Optical Kerr Effect and Imaging of Magnetic Octupole Domains in an Antiferromagnetic Metal*, Nat. Photonics **12**, 73 (2018).

[30] J. Xu, C. Zhou, M. Jia, D. Shi, C. Liu, H. Chen, G. Chen, G. Zhang, Y. Liang, and J. Li, *Imaging Antiferromagnetic Domains in Nickel-Oxide Thin Films by Magneto-Optical Voigt Effect*, arXiv:1906.06844.

[31] I. Gross, W. Akhtar, V. Garcia, L. J. Martínez, S. Chouaieb, K. Garcia, C. Carrétéro, A. Barthélémy, P. Appel, P. Maletinsky, J. V. Kim, J. Y. Chauleau, N. Jaouen, M. Viret, M. Bibes, S. Fusil, and V. Jacques, *Real-Space Imaging of Non-Collinear Antiferromagnetic Order with a Single-Spin Magnetometer*, Nature (London) **549**, 252 (2017).

[32] M. Ikhlas, T. Tomita, T. Koretsune, M.-T. Suzuki, D. Nishio-Hamane, R. Arita, Y. Otani, and S. Nakatsuji, *Large Anomalous Nernst Effect at Room Temperature in a Chiral Antiferromagnet*, Nat. Phys. **13**, 1085 (2017).

[33] S. M. Wu, W. Zhang, K. C. Amit, P. Borisov, J. E. Pearson, J. S. Jiang, D. Lederman, A. Hoffmann, and A. Bhattacharya, *Antiferromagnetic Spin Seebeck Effect*, Phys. Rev. Lett. **116**, 097204 (2016).

[34] S. Seki, T. Ideue, M. Kubota, Y. Kozuka, R. Takagi, M. Nakamura, Y. Kaneko, M. Kawasaki, and Y. Tokura, *Thermal Generation of Spin Current in an Antiferromagnet*, Phys. Rev. Lett. **115**, 266601 (2015).

[35] M. Weiler, M. Althammer, F. D. Czeschka, H. Huebl, M. S. Wagner, M. Opel, I.-M. Imort, G. Reiss, A. Thomas, R. Gross, and S. T. B. Goennenwein, *Local Charge and Spin Currents in Magnetothermal Landscapes*, Phys. Rev. Lett. **108**, 106602 (2012).

[36] J. M. Bartell, D. H. Ngai, Z. Leng, and G. D. Fuchs, *Towards a Table-Top Microscope for Nanoscale Magnetic Imaging Using Picosecond Thermal Gradients*, Nat. Commun. **6**, 8460 (2015).

[37] F. Guo, J. M. Bartell, D. H. Ngai, and G. D. Fuchs, *Phase-Sensitive Imaging of Ferromagnetic Resonance Using Ultrafast Heat Pulses*, Phys. Rev. Applied **4**, 044004 (2015).

[38] F. Guo, J. M. Bartell, and G. D. Fuchs, *Ferromagnetic Resonance Phase Imaging in Spin Hall Multilayers*, Phys. Rev. B **93**, 144415 (2016).

[39] J. M. Bartell, C. L. Jermain, S. V. Aradhya, J. T. Brangham, F. Yang, D. C. Ralph, and G. D. Fuchs, *Imaging Magnetization Structure and Dynamics in Ultrathin* $Y_3Fe_5O_{12}/Pt$ *Bilayers with High Sensitivity Using the Time-Resolved Longitudinal Spin Seebeck Effect*, Phys. Rev. Applied **7**, 044004 (2017).

[40] F. B. Lewis and N. H. Saunders, *The Thermal Conductivity of NiO and CoO at the Néel Temperature*, J. Phys. C **6**, 2525 (1973).

[41] G. A. Slack, *Crystallography and Domain Walls in Antiferromagnetic NiO Crystals*, J. Appl. Phys. **31**, 1571 (1960).

[42] E. Uchida, N. Fukuoka, H. Kondoh, and T. Takeda, *Magnetic Anisotropy of Single Crystals of NiO and MnO*, J. Phys. Soc. Jpn. **23**, 1197 (1967).

[43] S. Saito, M. Miura, and K. Kurosawa, *Optical Observations of Antiferromagnetic S Domains in NiO (111) Platelets*, J. Phys. C **13**, 1513 (1980).

[44] J. Stöhr, A. Scholl, T. J. Regan, S. Anders, J. Lüning, M. R. Scheinfein, H. A. Padmore, and R. L. White, *Images of the Antiferromagnetic Structure of a NiO(100) Surface by Means of X-Ray Magnetic Linear Dichroism Spectromicroscopy*, Phys. Rev. Lett. **83**, 1862 (1999).

[45] See Supplemental Material at http://link.aps.org/supplemental/10.1103/PhysRevX.9.041016 for structural

characterization of Pt/NiO and Pt/NiO/Pt, further control experiments establishing AF LSSE, and characterization of laser-induced heating.

[46] F. L. A. Machado, P. R. T. Ribeiro, J. Holanda, R. L. Rodríguez-Suárez, A. Azevedo, and S. M. Rezende, *Spin-Flop Transition in the Easy-Plane Antiferromagnet Nickel Oxide*, Phys. Rev. B **95**, 104418 (2017).

[47] K. Arai, T. Okuda, A. Tanaka, M. Kotsugi, K. Fukumoto, T. Ohkochi, T. Nakamura, T. Matsushita, T. Muro, M. Oura, Y. Senba, H. Ohashi, A. Kakizaki, C. Mitsumata, and T. Kinoshita, *Three-Dimensional Spin Orientation in Antiferromagnetic Domain Walls of NiO Studied by X-Ray Magnetic Linear Dichroism Photoemission Electron Microscopy*, Phys. Rev. B **85**, 104418 (2012).

[48] K. Uchida, S. Takahashi, K. Harii, J. Ieda, W. Koshibae, K. Ando, S. Maekawa, and E. Saitoh, *Observation of the Spin Seebeck Effect*, Nature (London) **455**, 778 (2008).

[49] C. M. Jaworski, J. Yang, S. Mack, D. D. Awschalom, J. P. Heremans, and R. C. Myers, *Observation of the Spin-Seebeck Effect in a Ferromagnetic Semiconductor*, Nat. Mater. **9**, 898 (2010).

[50] A. Kehlberger, U. Ritzmann, D. Hinzke, E.-J. Guo, J. Cramer, G. Jakob, M. C. Onbasli, D. H. Kim, C. A. Ross, M. B. Jungfleisch, B. Hillebrands, U. Nowak, and M. Kläui, *Length Scale of the Spin Seebeck Effect*, Phys. Rev. Lett. **115**, 096602 (2015).

[51] J. Xiao, G. E. W. Bauer, K. C. Uchida, E. Saitoh, and S. Maekawa, *Theory of Magnon-Driven Spin Seebeck Effect*, Phys. Rev. B **81**, 214418 (2010).

[52] J. Kimling, G.-M. Choi, J. T. Brangham, T. Matalla-Wagner, T. Huebner, T. Kuschel, F. Yang, and D. G. Cahill, *Picosecond Spin Seebeck Effect*, Phys. Rev. Lett. **118**, 057201 (2017).

[53] B. L. Giles, Z. Yang, J. S. Jamison, J. M. Gomez-Perez, S. Vélez, L. E. Hueso, F. Casanova, and R. C. Myers, *Thermally Driven Long-Range Magnon Spin Currents in Yttrium Iron Garnet due to Intrinsic Spin Seebeck Effect*, Phys. Rev. B **96**, 180412(R) (2017).

[54] Y. Ohnuma, H. Adachi, E. Saitoh, and S. Maekawa, *Spin Seebeck Effect in Antiferromagnets and Compensated Ferrimagnets*, Phys. Rev. B **87**, 014423 (2013).

[55] A. J. Sievers and M. Tinkham, *Far Infrared Antiferromagnetic Resonance in MnO and NiO*, Phys. Rev. **129**, 1566 (1963).

[56] J. Holanda, D. S. Maior, O. A. Santos, L. H. Vilela-Leão, J. B. S. Mendes, A. Azevedo, R. L. Rodríguez-Suárez, and S. M. Rezende, *Spin Seebeck Effect in the Antiferromagnet Nickel Oxide at Room Temperature*, Appl. Phys. Lett. **111**, 172405 (2017).

[57] S. M. Rezende, R. L. Rodríguez-Suárez, and A. Azevedo, *Diffusive Magnonic Spin Transport in Antiferromagnetic Insulators*, Phys. Rev. B **93**, 054412 (2016).

[58] S. A. Bender, H. Skarsvåg, A. Brataas, and R. A. Duine, *Enhanced Spin Conductance of a Thin-Film Insulating Antiferromagnet*, Phys. Rev. Lett. **119**, 056804 (2017).

[59] S. A. Bender and Y. Tserkovnyak, *Interfacial Spin and Heat Transfer between Metals and Magnetic Insulators*, Phys. Rev. B **91**, 140402(R) (2015).

[60] S. M. Rezende, R. L. Rodríguez-Suárez, and A. Azevedo, *Theory of the Spin Seebeck Effect in Antiferromagnets*, Phys. Rev. B **93**, 014425 (2016).

[61] I. Gray, G. M. Stiehl, J. T. Heron, A. B. Mei, D. G. Schlom, R. Ramesh, D. C. Ralph, and G. D. Fuchs, *Imaging Uncompensated Moments and Exchange-Biased Emergent Ferromagnetism in FeRh Thin Films*, arXiv:1906.07243.

[62] M. Charilaou and F. Hellman, *Roughness Effects in Uncompensated Antiferromagnets*, J. Appl. Phys. **117**, 083907 (2015).

[63] I. K. Schuller, R. Morales, X. Batlle, U. Nowak, and G. Güntherodt, *Role of the Antiferromagnetic Bulk Spins in Exchange Bias*, J. Magn. Magn. Mater. **416**, 2 (2016).

[64] H. Nakayama, M. Althammer, Y.-T. Chen, K. Uchida, Y. Kajiwara, D. Kikuchi, T. Ohtani, S. Geprägs, M. Opel, S. Takahashi, R. Gross, G. E. W. Bauer, S. T. B. Goennenwein, and E. Saitoh, *Spin Hall Magnetoresistance Induced by a Nonequilibrium Proximity Effect*, Phys. Rev. Lett. **110**, 206601 (2013).

[65] G. R. Hoogeboom, A. Aqeel, T. Kuschel, T. T. M. Palstra, and B. J. van Wees, *Negative Spin Hall Magnetoresistance of Pt on the Bulk Easy-Plane Antiferromagnet NiO*, Appl. Phys. Lett. **111**, 052409 (2017).

[66] J. Fischer, O. Gomonay, R. Schlitz, K. Ganzhorn, N. Vlietstra, M. Althammer, H. Huebl, M. Opel, R. Gross, S. T. B. Goennenwein, and S. Geprägs, *Spin Hall Magnetoresistance in Antiferromagnet/Heavy-Metal Heterostructures*, Phys. Rev. B **97**, 014417 (2018).

[67] T. Moriyama, W. Zhou, T. Seki, K. Takanashi, and T. Ono, *Spin-Orbit-Torque Memory Operation of Synthetic Antiferromagnets*, Phys. Rev. Lett. **121**, 167202 (2018).

Supplemental Information for "Spin Seebeck imaging of spin-torque switching in antiferromagnetic Pt/NiO heterostructures"

Isaiah Gray,[1,2] Takahiro Moriyama,[3] Nikhil Sivadas,[1] Gregory M. Stiehl,[4] John T. Heron,[5] Ryan Need,[6] Brian J. Kirby,[6] David H. Low,[1] Katja C. Nowack,[4,2] Darrell G. Schlom,[7,2] Daniel C. Ralph,[4,2] Teruo Ono,[3] and Gregory D. Fuchs[1,2]

[1]*School of Applied and Engineering Physics, Cornell University, Ithaca NY 14853*

[2]*Kavli Institute for Nanoscale Science, Ithaca NY 14853*

[3]*Institute for Chemical Research, Kyoto University, Uji, Kyoto, 611-0011, Japan*

[4]*Department of Physics, Cornell University, Ithaca NY 14853*

[5]*Department of Materials Science and Engineering, University of Michigan, Ann Arbor, Michigan*

[6]*NIST Center for Neutron Research, National Institute of Standards and Technology, Gaithersburg, Maryland 20899*

[7]*Department of Materials Science and Engineering, Cornell University, Ithaca, NY 14853*

(Dated: September 10, 2019)

S1. EXPERIMENTAL DETAILS OF AF LSSE MICROSCOPY

Our measurement circuit, schematically shown in Figure S1, is similar to that described in [1] and [2]. We generate local heating with 3 ps-wide pulses from a Ti:Sapphire laser at 785 nm wavelength at a repetition rate of 76 MHz. We use a 0.9 NA optical microscope objective to focus the beam down to a 650 nm diameter spot. The laser pulse train produces a spin Seebeck voltage pulse train at the same repetition rate.

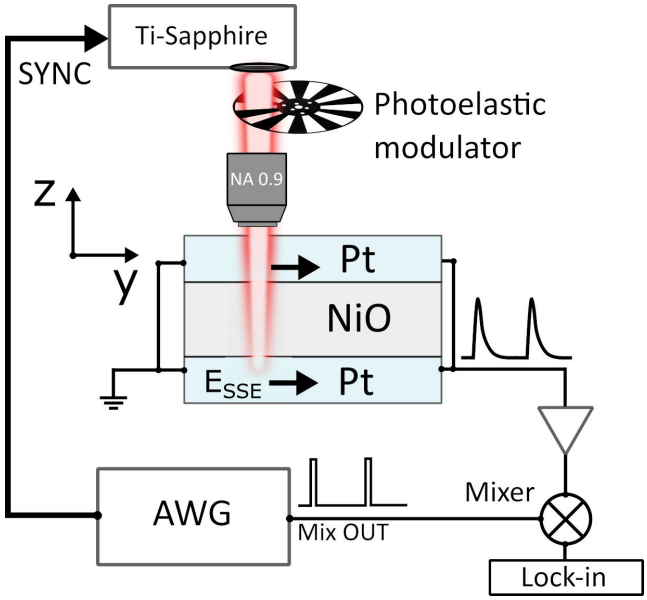

FIG. S1: Schematic of the measurement circuit. 3 ps-wide pulses from a Ti:Sapphire laser at 76 MHz repetition rate generate voltage pulses, which are amplified and mixed with a reference voltage pulse train from an arbitrary waveform generator (AWG). We modulate the laser intensity at 100 kHz with a photoelastic modulator (PEM) and detect the resulting voltage with a lock-in amplifier.

The duration of each voltage pulse is equal to the time duration of the interfacial temperature drop ΔT [1], which we estimate from the laser heating results in Fig. S11 to be $\sim$50 ps for the bilayer and $\sim$300 ps for the trilayer. We feed the pulses into a 50 Ω coplanar waveguide transmission line. After amplifying the pulses we perform homodyne detection by electrically mixing the pulses with a train of 600 ps-wide square pulses produced by an arbitrary waveform generator (AWG). Longer mixing pulses yield larger signal, but if the mixing pulses are too long the signal-to-noise decreases because we are more exposed to noise between thermal pulses. We have found 600 ps width to be a good compromise. We synchronize the laser repetition rate to the external AWG pulse train frequency using a

Coherent Synchro-lock AP 9th-harmonic locking mechanism inside the laser cavity. To take advantage of low-noise lock-in detection techniques, we modulate the intensity of the laser beam at 100 kHz with a photoelastic modulator and two polarizers. The lock-in signal at the end of this process is what we call in the main text $V_{AF\ LSSE}$.

Note that impedance mismatch between the sample resistance and the 50 Ω transmission line results in an overall signal scaling factor that depends on sample resistance, which ranges between 450 Ω and 650 Ω in our Hall crosses. To remove this dependence, all AF LSSE images, both in the main text and in the supplementary information, have been normalized by the factor $(R_{sample} + 50\ \Omega)/50\ \Omega$.

S2. STRUCTURAL CHARACTERIZATION OF Pt/NiO AND Pt/NiO/Pt

In the main text we image four sets of samples: the Pt/NiO(111) bilayer in Fig. 1 and Fig. 4, the NiO(111)/Pt and NiO(001)/Pt bilayers in Fig. 2, and the Pt/NiO(111)/Pt trilayer in Fig. 3. The Pt/NiO bilayer and the Pt/NiO/Pt trilayer are grown by magnetron sputtering on MgO(111) single-crystal substrates, similar to the samples in Ref. [3]. In the Pt/NiO/Pt trilayer the bottom Pt layer is deposited at 600 °C, while in the Pt/NiO bilayer the first nanometer of Pt is deposited at 600 °C before cooling to 400 °C for the remainder of the deposition. The 165 nm NiO(111)/Pt and 136 nm NiO(001)/Pt bilayers in Fig. 2 are grown by molecular beam epitaxy on $MgAl_2O_4$(111) and MgO(001) substrates, respectively. The $MgAl_2O_4$ is annealed at 900 °C before depositing NiO at 50 °C, and the MgO is annealed at 700 °C before depositing NiO at 500 °C.

In Fig. S2 we show *in-situ* RHEED taken during deposition, XRD, and XRR of the thin Pt/NiO bilayer and Pt/NiO/Pt trilayer. Although the NiO(111) layers are too thin to appear in the XRD, the RHEED shows epitaxial growth of each layer. Fig. S3 shows RHEED, XRD, and XRR of the thicker NiO(111) and NiO(001) samples, in which the NiO peaks are prominently visible. By fitting the XRR data we estimate the thickness of each layer and the surface roughness of each interface, from which we draw two important conclusions. First, we find that the NiO layer in the trilayer in Fig. S2(c) is thicker (13.6 nm) than the NiO layer in the bilayer in Fig. S2(b) (5.4 nm), which may explain the larger domain size in the AF LSSE images of the trilayer in Fig. 3 than of the Pt/NiO bilayer. Second, we find that the interfacial roughness of the 165 nm-thick NiO(111)/Pt sample

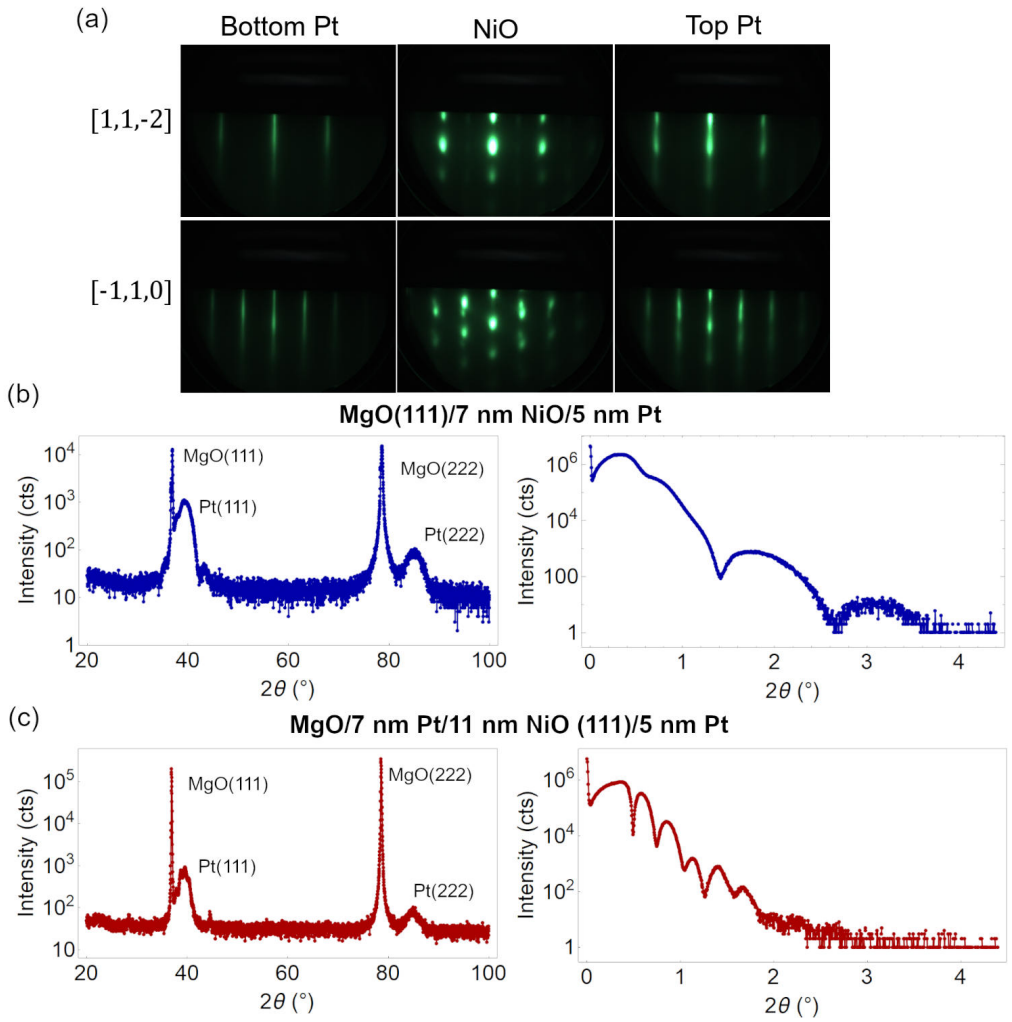

FIG. S2: (a) *In-situ* RHEED taken during deposition of the Pt/NiO/Pt trilayer in Fig. 3 of the main text, showing epitaxial growth of each layer. The NiO/Pt bilayer in Fig. 1 and 4 is grown similarly. (b, c) XRD and XRR scans of the NiO/Pt bilayer and Pt/NiO/Pt trilayer, respectively.

is slightly greater than the roughness of the 136 nm-thick NiO(001)/Pt sample – 1.0 nm compared to 0.2 nm – which we expect because the MgO(111) surface is generally rougher than the MgO(001) surface. This rules out the possibility that the lack of $V_{AF\ LSSE}$ signal from the NiO(001) sample in Fig. 2(b) compared to the NiO(111) sample in Fig. 2(a) is due to interface roughness.

S3. CHARACTERIZING SUBSTRATE ARTIFACTS IN AF LSSE IMAGES

In addition to antiferromagnetic domain contrast, the AF LSSE images of 6 nm-thick NiO in Fig. 1 and 4 and Fig. 3 to a lesser extent exhibit sharp straight lines that we attribute to

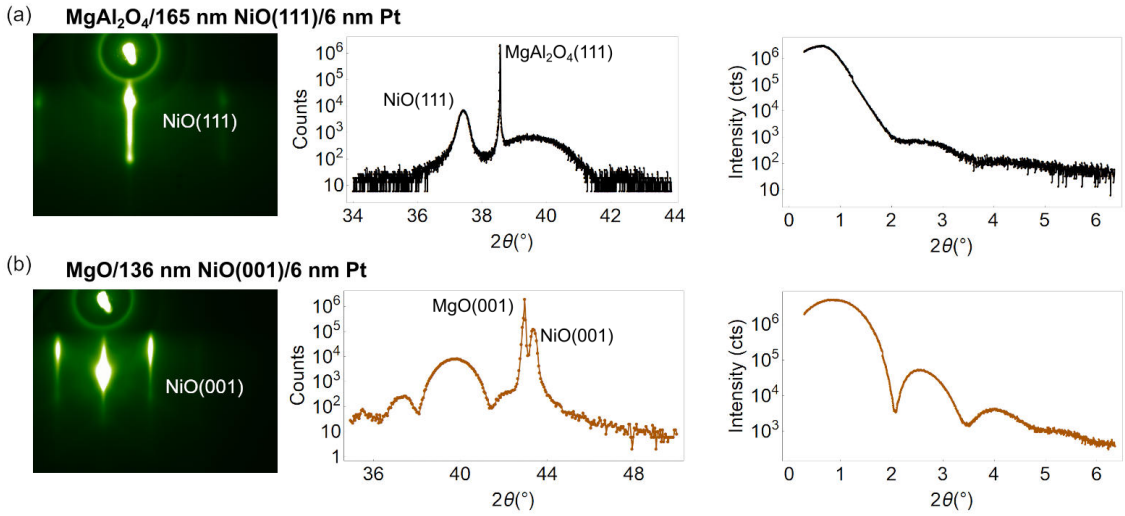

FIG. S3: (a, b) RHEED, XRD, and XRR scans of the 165 nm NiO(111)/Pt and 136 nm NiO(001)/Pt in Fig. 2 of the main text, respectively. By fitting the XRR we find that the interface roughness of the NiO(111)/Pt is 1.0 nm, greater than the 0.2 nm interface roughness of the NiO(001)/Pt. This rules out the possibility that the lack of $V_{AF\ LSSE}$ in NiO(001) compared to NiO(111) is due to interface roughness.

spatial nonuniformity in the MgO(111) substrate. Atomic force microscopy (AFM) images of a similar MgO(111) substrate in Fig. S4(a) show similar straight valleys, about 1 nm deep, which are consistent with scratches from polishing. In Fig. S4(b), (c), and (d) we show corresponding AF LSSE and AFM images of a NiO/Pt bilayer, a Pt/NiO bilayer, and a Pt/NiO/Pt trilayer, respectively. In all three cases we observe straight lines in the AF LSSE images, highlighted in black dashed line, with corresponding 1 nm valleys in the AFM images, highlighted in white dashed line.

Artifacts from height nonuniformity appear in the AF LSSE images due to the charge Seebeck effect. Away from a scratch, the NiO thickness is approximately uniform (0.5 nm roughness) and the sample surface is thermally isotropic in the plane. Therefore, conventional Seebeck voltages from laser-induced in-plane thermal gradients cancel in detail and do not contribute to the AF LSSE voltage signal. At a substrate scratch, however, there is a discontinuity in in-plane thermal conductivity. This results in a dipole-like artifact in the AF LSSE images with positive voltage on one side of the boundary and negative voltage on the other. Ordinary Seebeck artifacts are more prominent in AF LSSE images of Pt/NiO bilayers than in the images of NiO/Pt bilayers and Pt/NiO/Pt trilayers, which is reasonable because we expect the bottom Pt/NiO interface to be more sensitive to the substrate than

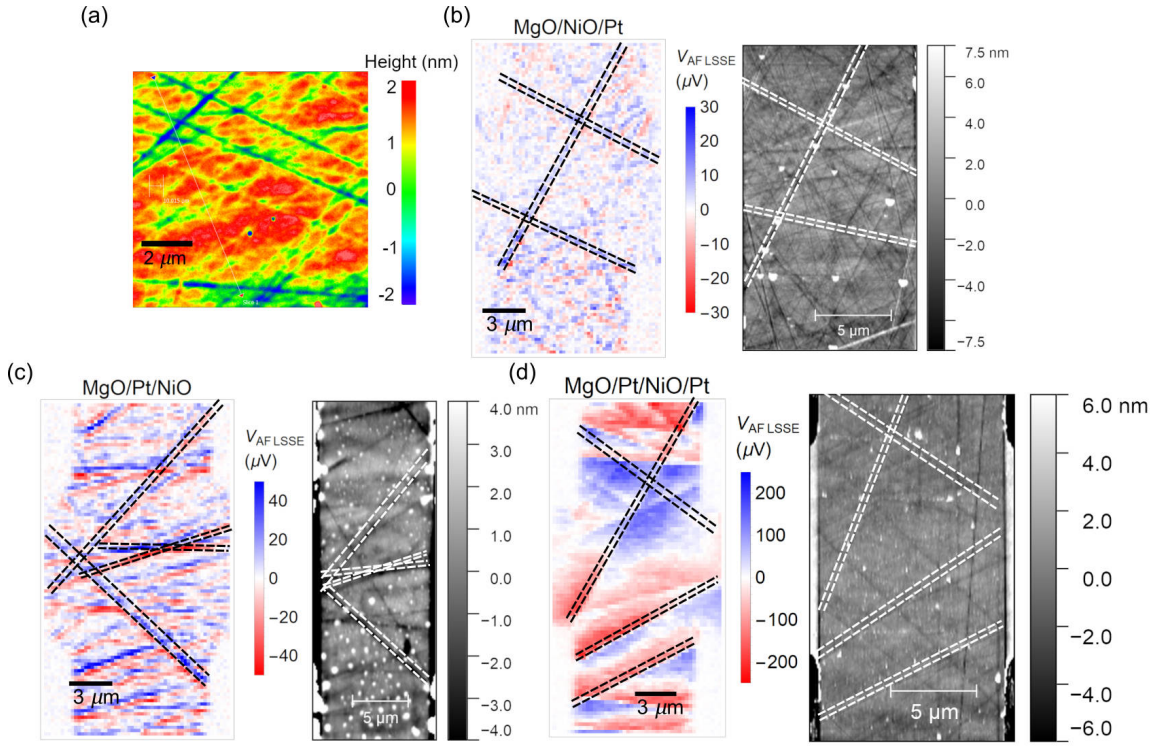

FIG. S4: Characterizing the effect of MgO(111) substrate roughness on the AF LSSE images. (a) AFM image of a MgO(111) substrate surface. Valleys in the shape of sharp diagonal lines reflect substrate morphology. (b, c, d) AF LSSE and AFM images of NiO/Pt, Pt/NiO, and Pt/NiO/Pt devices, respectively. Substrate scratches cause artifacts in the AF LSSE image from the charge Seebeck effect, visible as sharp lines with blue contrast on one side and red on the other. Substrate artifacts are more prominent in AF LSSE images of Pt/NiO samples than in images of NiO/Pt and Pt/NiO/Pt samples.

the top.

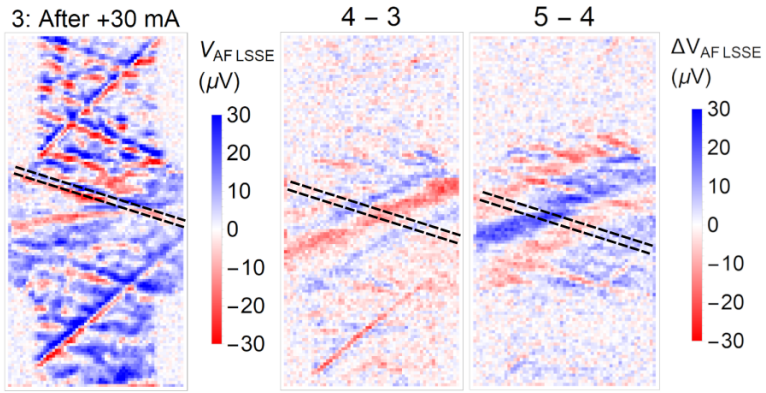

FIG. S5: Demonstrating that substrate scratches do not significantly affect the domain wall motion in Fig. 4 of the main text by superimposing the outline of the scratch on sequential difference images.

Based on the AF LSSE difference images in Fig. 3 and Fig. 4 of the main text, we conclude that the presence of substrate scratches does not significantly affect the AF switching in our samples. In Fig. 3, most of $\Delta V_{AF\ LSSE}$ occurs at a device corner, away from any scratches. By superimposing the outline of a sample scratch onto two difference images from Fig. 4, we show in Fig. S5 that the scratch disappears in the difference images and domain wall motion occurs nearly uninhibited across the scratch.

S4. CONTROL MEASUREMENTS ON NON-MAGNETIC Pt/MgO

We perform control images on non-magnetic 10 nm Pt/20 nm MgO, sputtered on sapphire, to check for other non-magnetic artifacts in our signal besides the conventional in-plane Seebeck effects from substrate scratches treated earlier. For example, high local current densities could create sample defects which could appear like switching in the AF LSSE images. We image 10 μm-wide Hall crosses of Pt/MgO at the same 3.4 mJ/cm^2 laser fluence we use for Pt/NiO in the main text, after applying similar current densities. Results are shown in Fig. S6. Note we make electrical contact to the bottom and right branches in an L-shape instead of the top and bottom contacts as in the Pt/NiO/Pt samples. This is done so that we can apply current along 45° diagonals with only two contacts.

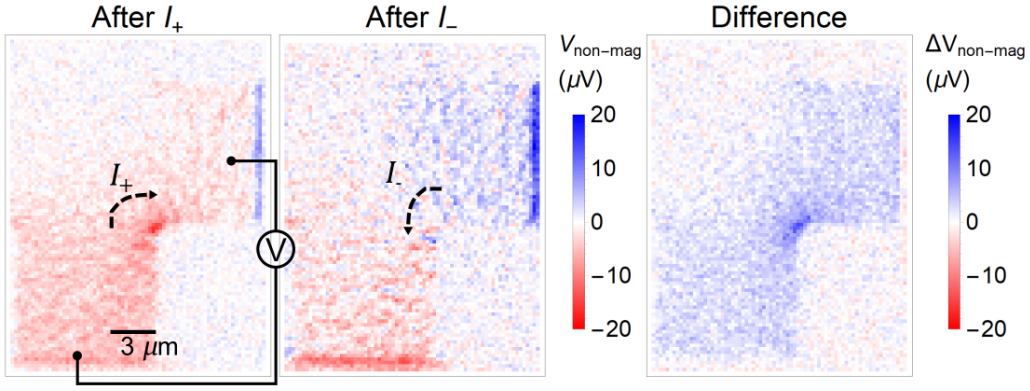

FIG. S6: Imaging 10 μm-wide Hall crosses of non-magnetic 10 nm Pt/20 nm MgO to check for non-magnetic artifacts in AF LSSE images. We make voltage contact to the bottom and right branch in an L-shape to apply current along 45° diagonals in the center. Non-magnetic contrast may be due to in-plane Seebeck voltages from local resistance fluctuations. We observe repeatable changes in contrast after applying 4×10^7A/cm^2 current density. Although the origin of the change in contrast is unknown, it is nearly uniform over the sample and does not exhibit localized domain rotation or domain wall motion.

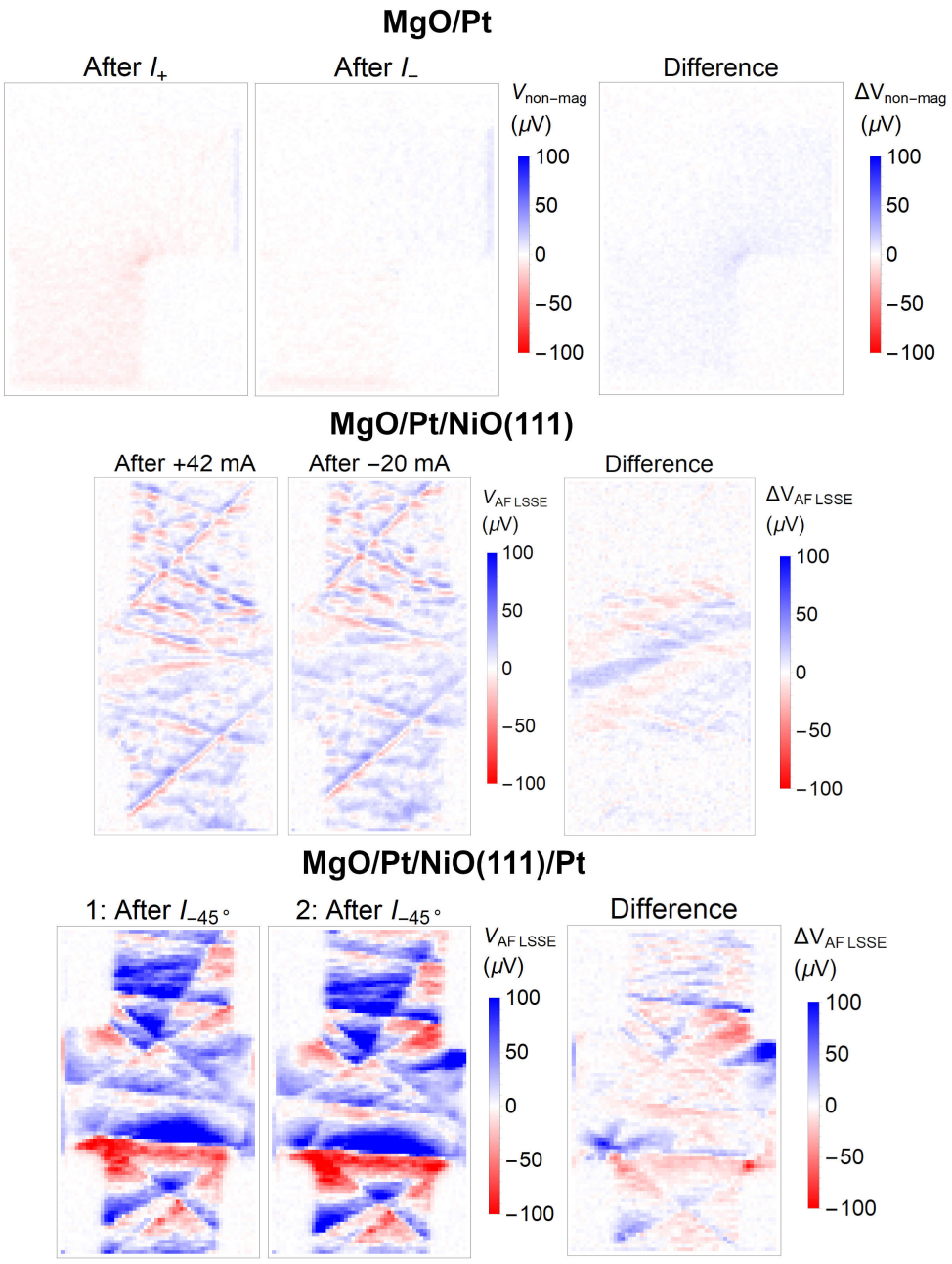

FIG. S7: Comparing the magnitude of (a) non-magnetic signal from Pt/MgO to AF LSSE signal from (b) the Pt/NiO bilayer in Fig. 1 and (c) the Pt/NiO/Pt trilayer in Fig. 3 of the main text by plotting them side-by-side on the same color scale. At the same fluence and current density, and normalizing by sample resistance, the magnitude of non-magnetic signal from Pt/MgO is a factor of 5-20 less than the magnitude of AF LSSE signal from Pt/NiO and Pt/NiO/Pt.

We observe submicron contrast which may represent local resistance fluctuations from surface roughness in the Pt layer, which we expect to be more prominent in the polycrys-

talline MgO/Pt samples than in the epitaxial Pt/NiO and Pt/NiO/Pt samples. Taking the difference after applying I_+ and I_-, we observe nearly spatially uniform changes in contrast, which are repeatable. Their origin is unknown: we speculate that they may be due to current-induced motion of sample defects. However, non-magnetic changes in contrast do not resemble local domain rotation or domain wall motion. In addition, the overall magnitude of the non-magnetic signal is about 5 times smaller than the AF LSSE signal from the Pt/NiO bilayer in Fig. 1 and 15-20 times smaller than the signal from the Pt/NiO/Pt trilayer in Fig. 4 of the main text. We show this in Fig. S7 by plotting images of MgO/Pt, Pt/NiO, and Pt/NiO/Pt all on the same color scale. We conclude that spurious non-magnetic signal does not contribute significantly to the AF LSSE images of NiO.

S5. TESTING FOR UNCOMPENSATED FM MOMENTS

We systematically check for uncompensated moments in our Pt/NiO/Pt samples that are distinct from the top and bottom uncompensated AF monolayers. These uncompensated moments would contribute to the $V_{AF\ LSSE}$ signal through a ferromagnetic spin Seebeck effect. Possible sources include bulk uncompensated moments in the NiO [4], interfacial uncompensated moments separate from the {111} interfacial uncompensated AF monolayers [5], canted moments at the Pt/NiO interfaces from symmetry breaking, and proximity-induced magnetization in the Pt. We first take AF LSSE images of a Pt/NiO/Pt sample at $\pm$250 mT, the largest field we can apply in our setup, as shown in Fig. S8. The AF LSSE signal is nearly pixel-for-pixel identical at $\pm$250 mT, which we expect since the spin-flop field in NiO is near 7 T [6] and the threshold field for domain motion is 1.5 T [7].

We perform polarized neutron reflectometry (PNR) on an unpatterned Pt/NiO/Pt film at room temperature to measure any overall magnetic moment in the film stack at 0.7 T applied field. The spin asymmetry plot is shown in Fig.S9. Within our sensitivity we measure no spin asymmetry and thus no net moment. We place an upper bound on the magnetization that could be present by modeling the expected spin asymmetry from a single polarized monolayer, which we choose in order to simulate uncompensated interfacial moments. We obtain a maximum magnetization of 0.75 μ_B/Ni, ruling out a fully magnetized (1.9 μ_B/Ni) monolayer.

Uncompensated moments could still be present if they are pinned by the Néel order and

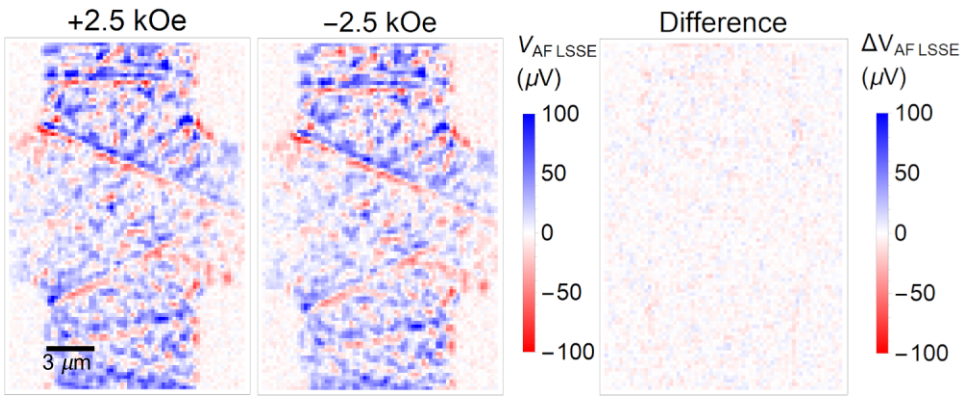

FIG. S8: AF LSSE images of a Pt/NiO/Pt sample at ±250 mT magnetic field. We observe no change in contrast within our sensitivity, which is consistent with an antiferromagnetic AF LSSE origin since the spin-flop field for NiO is 7 T and the threshold field for domain wall motion is 1.5 T.

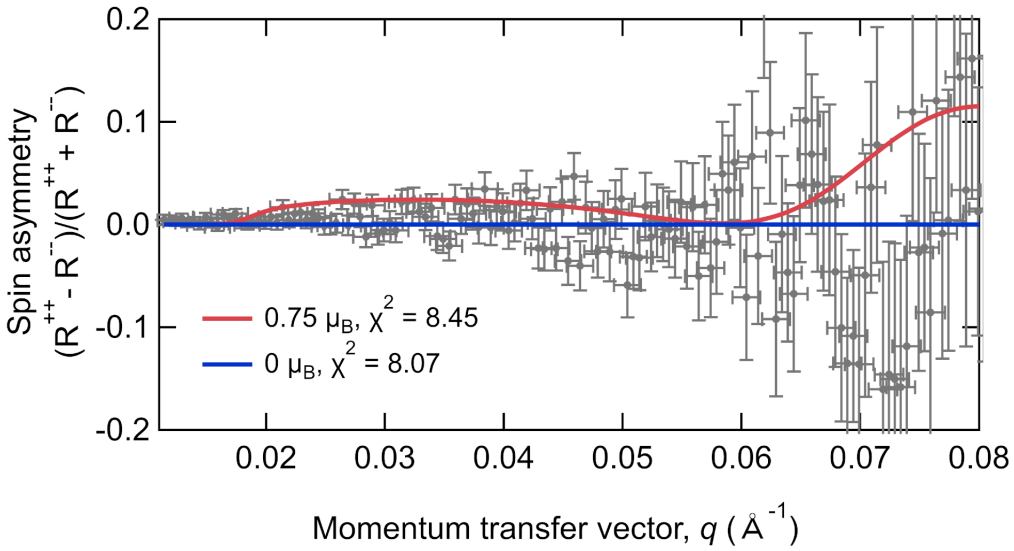

FIG. S9: The spin asymmetry plot from polarized neutron reflectometry on an unpatterned Pt/NiO/Pt film, performed at 295 K and 0.7 T applied field. No net moment is observed. From the noise level, we estimate an upper bound on the magnetization from one monolayer of 0.75 μ_B/Ni atom.

the Néel orientation averages to zero on the scale of microns to tens of microns. In Figure S10 we search for local moments by performing scanning SQUID microscopy, which directly images magnetic flux with ~ 1 μm resolution, on an annealed 10 μm-wide Pt/NiO/Pt Hall cross at a temperature of 7 K.

In Fig. S10(a) we locate the sample by imaging the flux while applying DC current through the vertical branch, and then in Fig. S10(b) we image the same region again with no current applied. The sample edges are outlined in white. Out-of-plane moments would

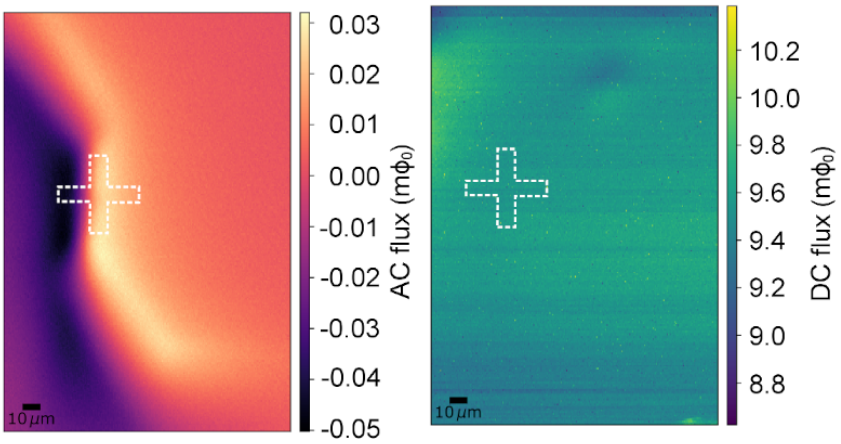

FIG. S10: Scanning SQUID images of a 10 μm-wide Pt/NiO/Pt Hall cross at 7 K, with ~ 1 μm resolution. (a) Magnetic flux generated by running 1 mA current through the sample. (b) Flux after turning off the current. The sample edges are outlined in white. From the lack of contrast observed, we estimate an upper bound of 8×10^{-4} μ_B/Ni local moment from a magnetized surface monolayer.

produce signal in the width of the channel, while in-plane moments would produce signal at the sample edges. However, Fig. S10(b) shows no contrast within sensitivity, so we do not measure any moment. By modeling the expected response from a magnetized surface monolayer, similarly to the PNR results, we calculate an upper bound of 8×10^{-4} μ_B/Ni. From this value we calculate a maximum bulk magnetization of 110 A/m, three orders of magnitude less than the 140 kA/m bulk magnetization of YIG at room temperature. The combination of insensitivity of the AF LSSE signal to magnetic field with null results from PNR and scanning SQUID leads us to conclude that the AF LSSE image signal originates from an antiferromagnetic spin Seebeck effect in NiO, rather than a ferromagnetic SSE from uncompensated moments.

S6. LASER-INDUCED HEATING IN Pt/NiO AND Pt/NiO/Pt

A. Temperature profile in Pt/NiO, NiO/Pt, and Pt/NiO/Pt samples

In this section we determine the laser-induced temperature profile in our Pt/NiO and Pt/NiO/Pt samples. Because we employ a picosecond pulsed laser for heating and detect $V_{AF\ LSSE}$ using a homodyne mixing circuit and a lock-in amplifier, directly measuring the transient temperature profile $T(r, z, t)$ is difficult. Therefore, we follow a procedure detailed

in our previous work [1, 2] to determine $T(r, z, t)$. We first simulate the laser-induced temperature profile using finite-element methods. Because the Pt and NiO are both much thinner than the optical absorption depths, the overall fraction of absorbed light is unknown and this requires calibration. We assume that the simulations determine $T(r, z, t)$ up to an overall scaling factor γ, which we determine experimentally. We first present the correctly scaled simulation results and then describe the experimental determination of γ.

We perform finite-element calculations of laser heating using the COMSOL Multiphysics® software package. We calculate the temperature profile by solving the radially symmetric heat diffusion equation, modeling the laser as a distributed heat source that exponentially decays with thickness. We employ absorption coefficients of 80.0 μm^{-1} for Pt and 6.0 $\times$ $10^{-2}\mu\text{m}^{-1}$ for NiO at 785 nm laser wavelength, taken from [8] and [9], respectively, which yield corresponding penetration depths of 12.5 nm and 170 μm. We assume 4 nm-thick Pt and 6 nm-thick NiO at a base temperature of 293.2 K.

In Fig. S11 we plot scaled simulated laser profiles for (a-c) NiO/Pt, (d-f) Pt/NiO, and (g-i) Pt/NiO/Pt samples at the 3.4 mJ/cm^2 fluence used in the AF LSSE images in the main text. We experimentally determined the scaling factor for a Pt/NiO bilayer similar to that in Fig. 1 of the main text; because the correction is only about 1%, we employed the same scaling factor for all three sets of samples. In all three samples, the thermal profile is dominated by temperature discontinuities at the Pt/NiO interfaces, which is due to interfacial thermal resistance [10]. In the simulations we assume an interfacial resistance between Pt and NiO of 2.0×10^{-3} K $\cdot$ m^2/MW, which is low even for lattice-matched epitaxial interfaces and thus probably an underestimation. Nevertheless, plotting the temperature depth profile at the beam center near peak heating in Fig. S11(b), (e), and (h) show that ΔT across each layer is between 3 and 5 K, while the temperature difference across the Pt/NiO interface ΔT_{int} can be tens of Kelvin. Although we do not know the values of the interface and bulk antiferromagnetic spin Seebeck coefficients, these profiles suggest that the interface AF LSSE is more strongly excited than a bulk AF LSSE.

In both the NiO/Pt and Pt/NiO bilayers, we observe that the Pt heats more than the NiO. From Fig. S11(b) and (e) the maximum laser-induced temperature increase of the Pt layer is about 90 K in the NiO/Pt sample and 70 K in the Pt/NiO sample, while the NiO layer only heats 10-15 K above room temperature. This is because the Pt directly absorbs laser light, while the NiO is nearly transparent to the 785 nm laser wavelength and is heated

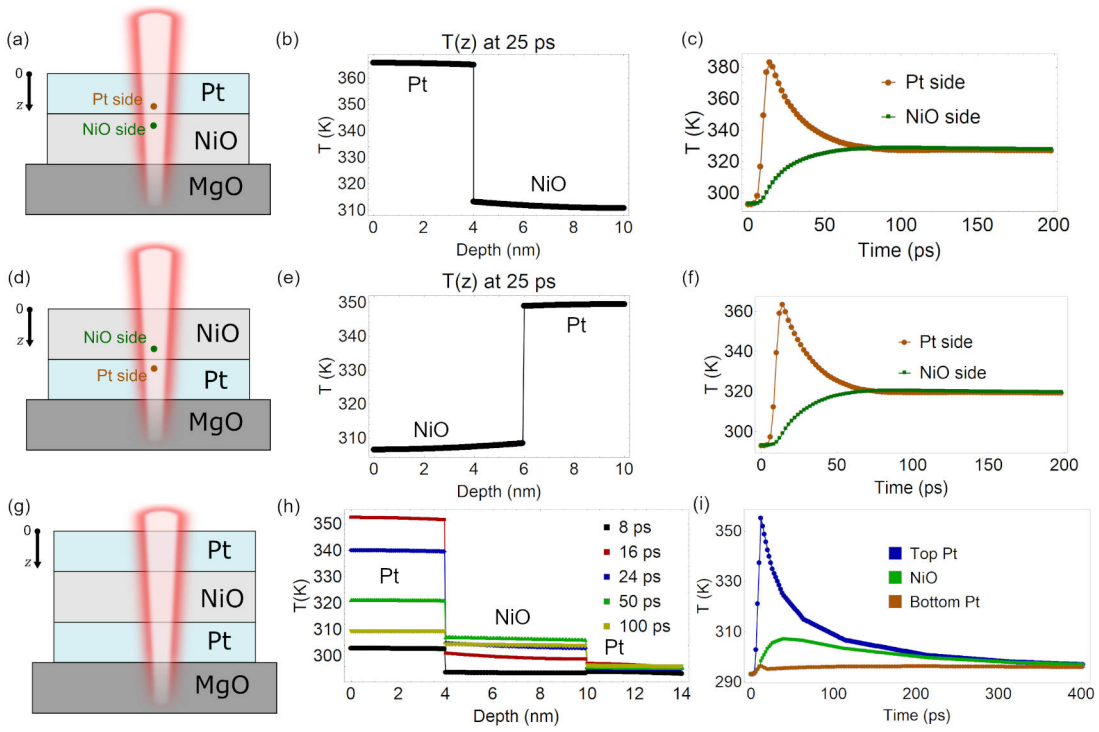

FIG. S11: Laser-induced heating in NiO/Pt, Pt/NiO, and Pt/NiO/Pt devices. (a) Schematic of the MgO/NiO/Pt bilayer. (b) Temperature profile at $r = 0$, $T(0, z)$, near peak heating at 25 ps. $T(r, z)$ is dominated by the temperature drop ΔT_{int} at the NiO/Pt interface. (c) Quantifying $\Delta T_{int}(t)$ by plotting $T(r = 0, t)$ for two points 0.5 nm above and below the interface. (d-f) The same as (a-c) for a Pt/NiO bilayer. In both bilayers, the Pt layer heats more than the NiO layer. (g) Schematic of the Pt/NiO/Pt trilayer. (h) $T(r = 0, z)$ in the trilayer for a series of times after the laser pulse arrival. (i) Average of $T(r = 0, z, t)$ across each layer. ΔT_{int} is greater across the top than the bottom NiO/Pt interface.

primarily by thermal contact with the Pt. We quantify ΔT_{int} for the bilayers in Fig. S11(c) and (f) by plotting $T(0, z, t)$ for two points 0.5 nm above and below the interface as a function of time. The Pt and NiO reach the same temperature after ∼50 ps, therefore the time duration of the $V_{AF\ LSSE}$ voltage pulses is ∼50 ps.

Because $T(r, z, t)$ in the trilayer is more complicated than $T(r, z, t)$ in the bilayers, we plot $T(0, z)$ of the trilayer for a series of times from 8 ps to 100 ps in Fig. S11(h). Due to absorption of laser light by the first Pt layer and reflections at the interfaces, the laser pulse only directly heats the bottom Pt layer by about 5 K. After 20 ps, the top Pt layer heats the NiO layer to a higher temperature than the bottom Pt layer. The temperature within each layer is nearly uniform, similar to the bilayer, therefore in Fig. S11 we plot the depth average of $T(0, z, t)$ for each layer as a function of time. The NiO remains hotter than the

bottom Pt layer until all three layers reach the same temperature after 300 ps.

B. Determining the scaling factor for the simulations

We determine the scaling factor for the simulations as follows: we convert the simulated laser-induced $T(r, z, t)$ into a transient resistance change $R(t)$ using the measured temperature dependence of resistance $R(T)$ in a Pt/NiO bilayer. We calculate the resulting lock-in voltage after mixing $V_{LI}^{sim}(I_{DC})$ as a function of DC current I_{DC}. We then experimentally measure $V_{LI}^{meas}(I_{DC})$ in the same sample and multiply $T(r, z, t)$ by a scaling factor γ so that $V_{LI}^{sim}(I_{DC})$ matches $V_{LI}^{meas}(I_{DC})$.

We first measure electrical resistance as a function of temperature $R(T)$ in a Pt/NiO device from the same chip as the sample in Fig. 1 and Fig. 4 of the main text, shown in Fig. S12(a). We fit to $R(T) = R_{293\ K} + \alpha T$, obtaining $\alpha = 0.58\ \Omega/K$. Using this data we convert $T(r, z, t)$ into a transient resistance change $R(t)$ over the whole device, taking into account the beam spot and sample dimensions. When a DC current I_{DC} is applied to the Pt/NiO bilayer during laser heating, the $R(t)$ produces a voltage $I_{DC}R(t)$ in addition to. The total voltage in the time domain is therefore

$$V_{total}(t) = V_{AF\ LSSE}(t) + I_{DC}R(t). \tag{1}$$

We show in [1] that after amplification and mixing with the reference pulse train $V_{ref}(t)$, the resulting lock-in voltage is

$$V_{LI} = \frac{1}{V_0} \sum_{k=-f_{max}/f_0}^{f_{max}/f_0} c_{-k}^{r}(c_k^{AF\ LSSE} + I_{DC}c_k^{\Delta R}), \tag{2}$$

where V_0 is a multiplicative factor accounting for the amplifier gain and transfer coefficient of the collection circuit, $f_{max} = 3$ GHz is the frequency bandwidth of the amplifiers, $f_0 = 76$ MHz is the laser repetition rate, $c_{-k}^{r} = \frac{1}{T}\int_0^T dt\ V_{ref}(t)\ e^{-2\pi ikt/T}$ is the Fourier component of the reference pulse train, $T = 1/f_0 = 13$ ns is the laser period, and $c_k^{AF\ LSSE}$ and $c_k^{\Delta R} = \frac{1}{T}\int_0^T dt\ \Delta R(t)\ e^{-2\pi ikt/T}$ are the Fourier components of $V_{AF\ LSSE}(t)$ and $\Delta R(t)$, respectively. Since c_{-k}^{r} is constant and $c_k^{AF\ LSSE}$ is approximately constant with I_{DC}, given V_0 and $R(t)$ we can calculate $V_{LI}(I_{DC})$.

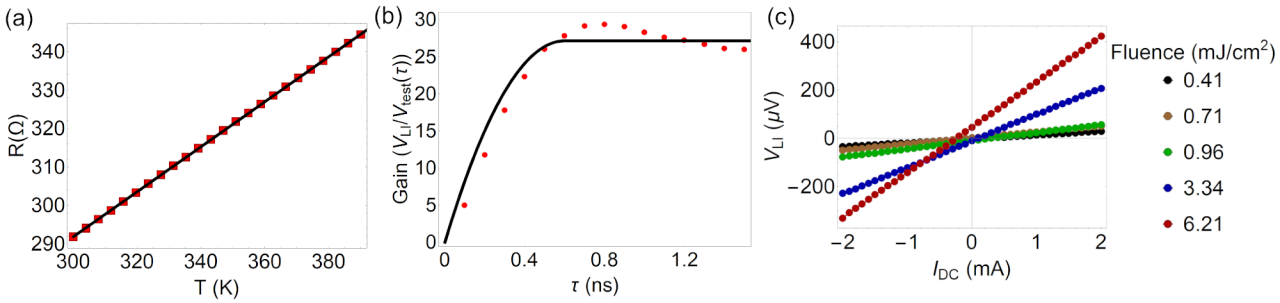

FIG. S12: (a) Resistance vs temperature $R(T)$ in a MgO/Pt/NiO bilayer. (b) Calibrating the transfer coefficient of the collection circuit. We apply a test pulse train V_{test} and measure the response V_{LI} as a function of V_{test} pulse width τ. (c) Measured lock-in signal V_{LI} while applying DC current I_{DC} in the same sample as in (a), at several different fluences.

To determine the constant factor V_0, we calibrate the transfer coefficient of the collection circuit by measuring the response V_{LI} to a known pulse train V_{test} with pulse width τ. Since we cannot directly generate ∼50 ps-wide pulses with our electronics, we instead measure V_{LI} as a function of τ down to $\tau = 100$ ps, the shortest pulse we can generate, and extrapolate. In Fig. S12(b) we plot the gain V_{LI}/V_{test} and the fit to Eqn. 2(c) with V_0 as the only free parameter. From this we extract $V_0 = (0.42 \pm 0.01)\ \mu$V.

After calculating $V_{LI}^{sim}(I_{DC})$ taking V_0 into account, we measure $V_{LI}(I_{DC})$ in the same sample as Fig. S12(a) in Fig. S12(c). We measure $V_{LI}^{meas}(I_{DC})$ at several different fluences so that we can determine $T(r, z, t)$ as a function of fluence f. At the range of I_{DC} used, both V_{LI}^{sim} and V_{LI}^{meas} are linear in I_{DC}. We therefore multiply $T(r, z, t)$ by the scaling factor γ so that the slope V_{LI}^{sim}/I_{DC} is equal to the slope V_{LI}^{meas}/I_{DC}. We experimentally determine a scaling factor of $\gamma = 1.01$. Because $T(r, z, t)$ is linear in f, γ is the same for all fluences in Fig. S12(c).

S7. EFFECTS OF HEATING AND LASER FLUENCE ON AF DOMAIN STRUCTURE

In this section we determine the effects of both global heating and local laser-induced heating on the AF domain structure of Pt/NiO and Pt/NiO/Pt samples. In three control experiments we perform $V_{AF\ LSSE}$ imaging as a function of temperature up to 110 °C, image before and after heat treatment at 200 °C, and image as a function of laser fluence f. We find that heating effects (both global and local) are irreversible and spatially distinct from

the domain rotation and domain wall motion produced by spin-torque switching.

A. Temperature-dependent AF LSSE images and effects of heat treatment

One of the studies of spin-torque switching in Pt/NiO [11] suggests that the switching is thermally activated, while recent works comparing spin-torque-induced and field-induced switching in Pt/α-Fe_2O_3 heterostructures [12, 13] highlight potential contributions to switching from anisotropic thermal expansion as well as potential heating-induced artifacts. We therefore determine the effects of global heating on $V_{AF\ LSSE}$ and the AF domain structure by imaging a Pt/NiO/Pt trilayer as a function of temperature in Fig. S13 up to 110 °C, the highest temperature we can achieve in our setup.

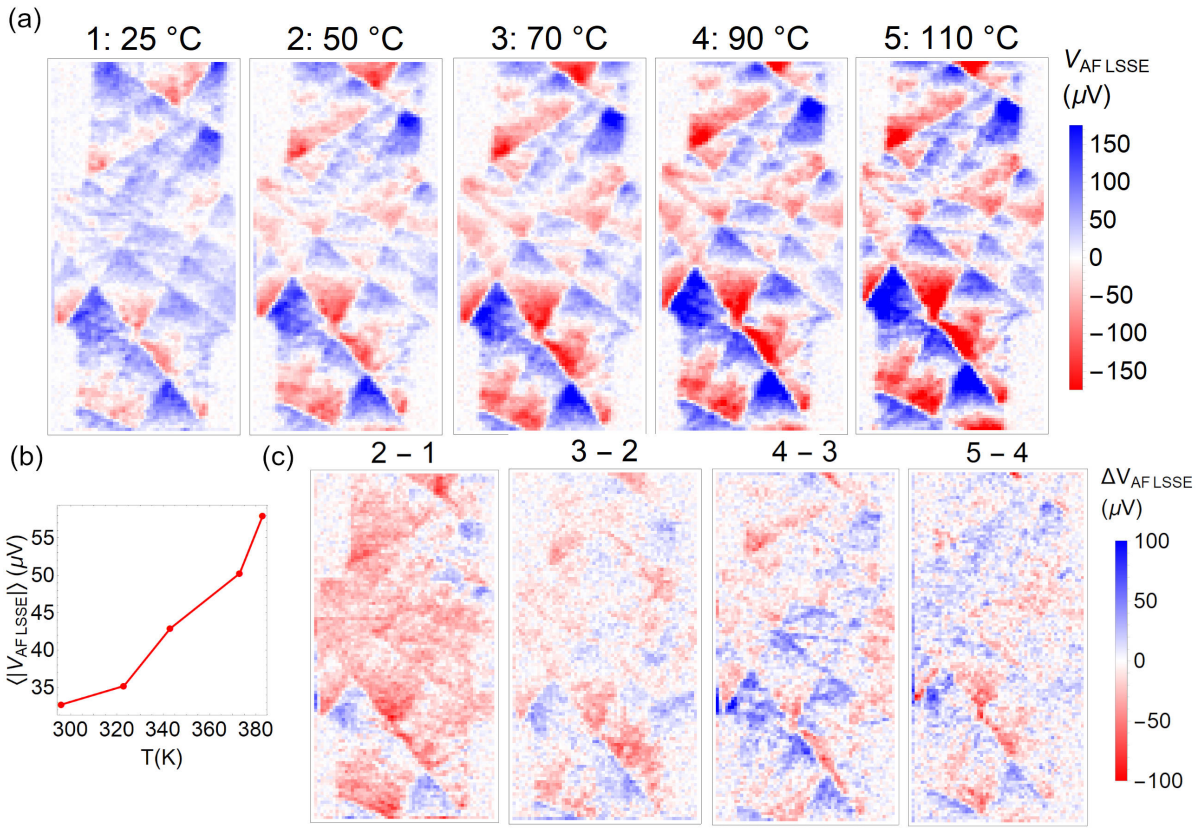

FIG. S13: (a) AF LSSE images of a Pt/NiO/Pt trilayer as a function of bath temperature. (b) Average $\langle V_{AF\ LSSE}\rangle$ of the absolute value of the pixels of each image in (a) as a function of T. (c) Sequential differences between the images in (a), showing heating-induced changes in AF domain structure.

We first note from the AF LSSE images in Fig.S13(a) that $V_{AF\ LSSE}$ increases with increasing T. One contribution to this increase is the spin Hall angle θ_{SHE}, which is linear

in electrical resistivity ρ. From Fig. S12(a), $\rho(T)$ is accurately modeled by $\rho(T) = \rho_{293\ K} + \alpha T$ with $\alpha = 0.58\ \Omega/\mathrm{K}$. To determine if $\rho(T)$ is sufficient to explain the temperature dependence of $V_{AF\ LSSE}$, we take the absolute value of the pixels in each image, compute the average of these absolute values, and plot this average as a function of temperature in Fig. S13(b). Comparing $\langle V_{AF\ LSSE}(T) \rangle$ to $R(T)$ in Fig. S12(b), we find from $T = 293$ K to 383 K, $V_{AF\ LSSE}$ increases by $\Delta V_{AF\ LSSE}/V_{AF\ LSSE}(293\ \mathrm{K}) = 44\%$ while $R(T)$ and therefore $\rho(T)$ increases by $\Delta R/R(293\ \mathrm{K}) = 22\%$. Increased θ_{SHE} from $\rho(T)$ is therefore not sufficient to explain the temperature dependence of $V_{AF\ LSSE}$.

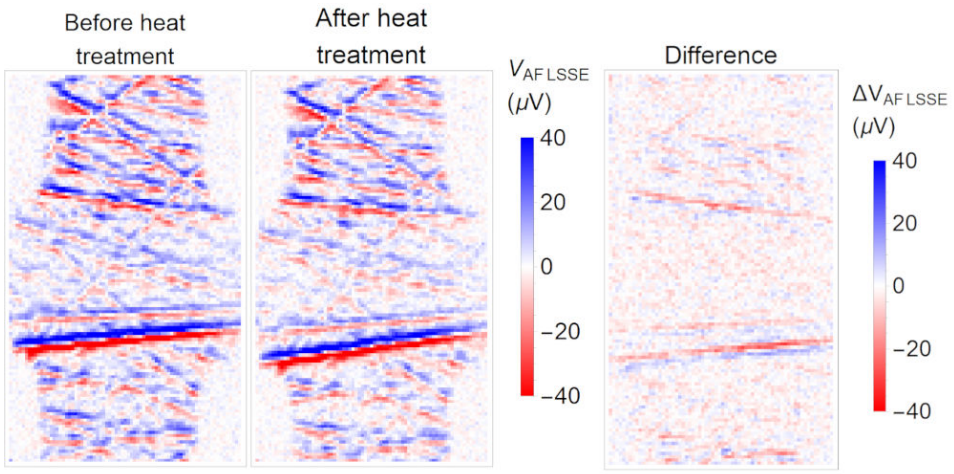

FIG. S14: AF LSSE images of a Pt/NiO bilayer at 25 °C before and after annealing the sample at 200 °C for 20 minutes. Unlike the sample in Fig. S13, we do not see significant changes in AF domain structure with heat treatment in this sample.

In Fig. S13(c) we plot sequential differences between the images in (a). If $V_{AF\ LSSE}$ increased uniformly with T the structure of each difference image would be the same as the AF LSSE images themselves. Instead we find that difference image shows different structure, and we see the most change from 25 °C to 50 °C, which shows that heating changes the domain structure. From the finite-element simulations in Fig. S23, we estimate ∼50 K heating of the NiO layer at 5×10^7 A/cm^2 writing current density. Therefore, current-induced heating may contribute to some of the switching images in Fig. 3 and Fig. 4 of the main text. However, we find that heating effects are almost uniformly distributed over the whole sample, and they are irreversible. Heating effects do not account for the back-and-forth domain rotation in Fig. 3 or the localized, current polarity-dependent domain wall motion in Fig. 4.

For completeness, we note that heating does not alter the AF domain structure in all our samples. In Fig. S14 we plot AF LSSE images of a Pt/NiO bilayer at 25 °C before and after annealing at 200°C for 20 minutes. No obvious change in domain structure is visible; weak contrast near ordinary Seebeck artifacts in the difference image likely reflect imperfect image alignment. Further studies are necessary to determine why some samples are affected by heating and others are not.

B. Effects of laser heating

In this section we determine the effect of laser fluence on $V_{AF\ LSSE}$ and the AF domain structure in a Pt/NiO/Pt sample. We demonstrate that at the fluences used in the main text, laser heating does not cause changes in the AF domain structure that would confound our interpretation of switching.

In Fig. S15(a) we perform AF LSSE imaging on a 10 μm-wide Pt/NiO/Pt sample as a function of laser fluence. From 1.8 mJ/cm^2 to 5.6 mJ/cm^2, we find that $V_{AF\ LSSE}$ increases uniformly over the whole sample and the spatial structure of the AF domains is unaffected. This series indicates that in the AF LSSE images in the main text, acquired using 3.4 mJ/cm^2 fluence, the laser probes the Néel order without perturbing it.

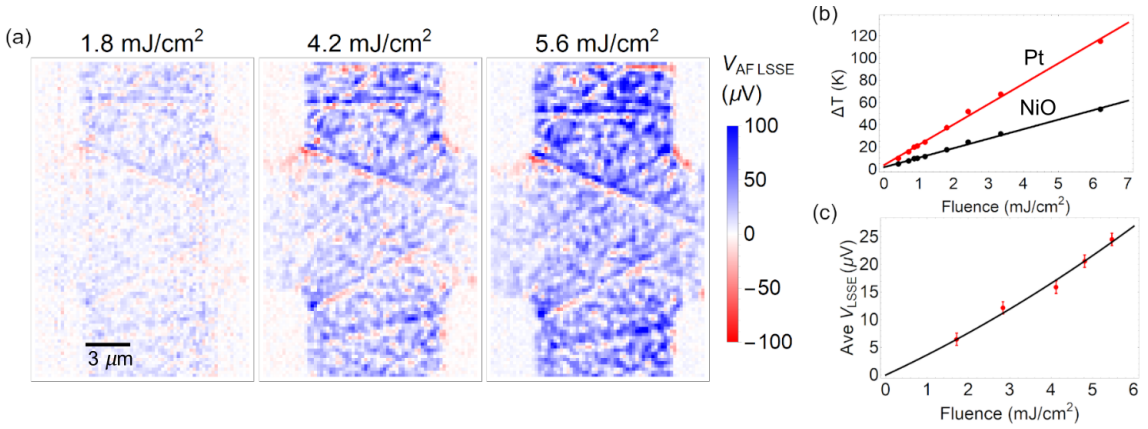

FIG. S15: (a) AF LSSE images of a 10 μm-wide Pt/NiO/Pt Hall cross at 3 different laser fluences. $V_{AF\ LSSE}$ increases but the AF domain structure is unchanged. (b) Maximum temperature increase of the Pt and NiO layers in a NiO/Pt bilayer as a function of fluence f. (c) Average $V_{AF\ LSSE}$ of the device in (a) as a function of f. We fit $\langle V_{AF\ LSSE}\rangle$ to $af + bf^2$.

There are two contributions to increased $V_{AF\ LSSE}$ with increasing fluence f. First, the

thermal spin current $\boldsymbol{J}_s$ is linear in the temperature difference ΔT_{int} across the Pt/NiO interface, which in turn is linear in laser heating power P and therefore fluence f. In Fig. S15(b) we plot the maximum temperature increase for both the Pt and NiO surfaces as a function of f. We obtain these plots by measuring the scaling factor γ mentioned in section S6 as a function of f. Second, the inverse spin Hall voltage $V_{AF\ LSSE}$ is linear in the spin Hall angle in Pt σ_{SHE}, which contains the electrical resistivity $\rho_{Pt}(T)$. In our devices we find above near room temperature the resistance $R(T)$ is well approximated by $R(T) \approx R_0 + \alpha T$ with $\alpha = 0.58\ \Omega/\mathrm{K}$. We therefore expect two contributions to $V_{AF\ LSSE}$, one linear and one quadratic in f. In Fig. S15 we plot the average of $V_{AF\ LSSE}$ over the whole device as a function of f fitted to the formula $V_{AF\ LSSE} = af + bf^2$. We obtain $a = 4.6 \pm 0.5\ \mu\mathrm{V} \cdot \mathrm{cm}^2/\mathrm{mJ}$ and $b = 0.2 \pm 0.1\ \mu\mathrm{V} \cdot \mathrm{cm}^4/\mathrm{mJ}^2$, which shows that $V_{AF\ LSSE}$ is nearly linear in f at the fluences employed in our samples.

To observe the effect of heating on the AF domain structure at high fluences, we then repeatedly image at 5.6 mJ/cm^2 laser fluence, which heats the NiO layer by ∼50 K as shown in Fig. S15(b). In Fig. S16 we plot the initial image (**1**), an image after scanning the laser over the sample 4 times without applying current (**2**), another image taken immediately afterwards (**3**), and the image differences (**2** − **1** and **3** − **2**).

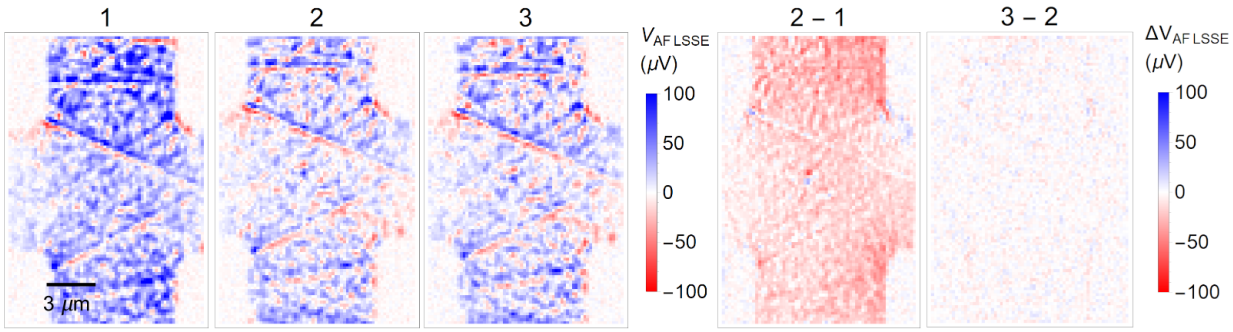

FIG. S16: Repeated imaging of a 10 μm-wide Pt/NiO/Pt Hall cross at 5.6 mJ/cm^2 fluence, which from Fig. S15((b) results in an estimated maximum $\Delta T = 50$ K at the top NiO surface. Repeated laser heating appears to cause the domains to locally reorient into local lowest-energy configurations, after which they do not rotate further.

We observe mostly blue contrast in **1**, which indicates that most of the AF domains have positive N_x projection. After repeatedly scanning the laser, we see approximately equal proportion of positive and negative N_x in **2**. **3** is nearly pixel-for-pixel identical to **2**, which means that the laser has no further effect after **2**. From this data we conjecture that

heating may locally destabilize the Néel order, causing the AF domains to reorient until they settle into local lowest-energy configurations (which are overall randomly oriented) and do not further rotate. This process is irreversible and occurs almost uniformly over the whole sample (seen in $\mathbf{2-1}$), quite different from the localized domain rotation and domain wall motion produced by spin-torque switching.

In conclusion, at 5.6 mJ/cm^2 fluence – which we estimate to heat the NiO layer by 50 K – and above, laser heating has a similar effect on the AF domains as global heating: it "randomizes" the in-plane orientation of the AF domains, and its effects occur over the whole sample and are irreversible. At 3.4 mJ/cm^2, the fluence used in the main text, laser heating does not affect the AF domain structure. Based on these two findings, we conclude that laser heating does not significantly affect the images of spin-torque-induced domain rotation and domain wall motion in the main text.

S8. EFFECTS OF ROUGHNESS AND TWO Pt/NiO INTERFACES ON THE AF LSSE SIGNAL

A. Effects of interfacial roughness at the Pt/NiO interface

Here we discuss the interfacial AF LSSE in the context of real samples, with surface and interface roughness. Non-magnetic artifacts from surface roughness or Pt thickness variations can be distinguished from AF LSSE signal by taking difference images, as we do in the main text. Local height variations in the NiO [14] could have a greater effect on the overall AF LSSE signal because an atomic step of one monolayer could cause $\boldsymbol{J}_s$ from the AF LSSE to locally reverse direction, as shown in Fig. S17. We distinguish two possible effects of random height variation depending on its lateral length scale. If the lateral length scale of surface roughness is much less than the 650 nm laser spot size, the laser averages over the roughness, as shown in Fig. S17(a). From AFM scans, we estimate the surface height variation to be about 1 nm, or 2-3 unit cells, and the lateral length scale of the height variation to be tens of nanometers. Although the sign of the averaged signal depends on the exact distribution of the height steps, the presence of atomic steps at the nanometer scale does not fundamentally alter the interpretation of the AF LSSE voltage as reporting N_x with a consistent sign inside AF domains.

If the lateral scale of height variation is comparable to or greater than the laser spot size – in other words, if the average thickness varies from pixel to pixel, as illustrated in Fig. S17(b), we would expect the AF LSSE voltage to contain contributions from both the spin structure and local thickness variations, which would manifest as nonuniformity and sign changes in the AF LSSE signal within a single AF domain.

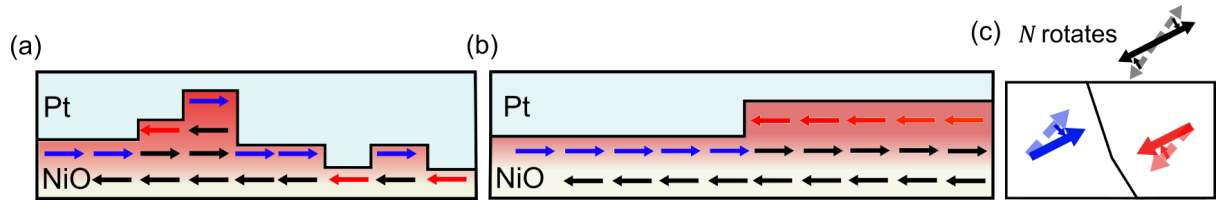

FIG. S17: Potential effects of surface roughness on the AF LSSE signal. Region 1 shows the ideal, atomically flat interface. Region 2 represents roughness in the form of random atomic steps, which decreases the overall signal but does not change its interpretation. Region 3 shows a flat interface with an average height one monolayer different than Region 1, resulting in the opposite sign in the AF LSSE signal within the same S-domain.

We argue that local thickness variations does not significantly contribute to the AF LSSE signal. First, the trilayer samples in Fig. 3 in the main text, as well as those shown in S4, contain AF domains that are 3-10 μm wide. From AFM images, we know that the sample thickness is not uniform to within one monolayer over a distance of several μm. Therefore, if thickness variations made a significant contribution to our signal, we would expect to observe signal variation, including sign changes, inside the AF domain. Instead, we find that $V_{AF\ LSSE}$ maintains a consistent sign within AF domains.

Second, AF LSSE contrast from thickness variations would exhibit characteristic switching patterns that we do not observe. In Fig. S17(c) we illustrate how a uniform AF domain containing a thickness step of one monolayer (the most extreme case) would respond under domain rotation. Upon first imaging, we would obtain a sign reversal as the probe crosses the step. After imaging domain rotation from spin torque, we expect ΔV_{AFLSSE} in the two regions to be anticorrelated – if the blue region becomes bluer, the red region should become redder, and vice versa. Therefore, if signal contrast were dominated by interfacial steps, the difference image should inherit the pixel-to-pixel nonuniformity of the AF LSSE images. In the AF switching images in Fig. 4 of the main text, we see the opposite effect: the difference images are more uniform than the AF LSSE images themselves. Within the

region labeled *domain rotation*, blue domains become more blue and red domains less red, corresponding to a uniform increase in N_x. In addition, thickness variations would not move under applied current, therefore the domain wall motion and domain expansion in Fig. 4 of the main text is not due to surface roughness. Based on these reasons, we conclude that in our samples $V_{AF\ LSSE}$ is due to spin contrast and not surface roughness. Further studies, perhaps comparing different growth methods, are necessary to elucidate the role of surface roughness in interfacial AF LSSE.

B. Effects of two Pt/NiO interfaces on the AF LSSE signal

In the Pt/NiO/Pt trilayers, both Pt/NiO interfaces can contribute to the $V_{AF\ LSSE}$ we measure. Even though the simulations of laser heating in Fig. S11 suggest that ΔT_{int} across the top interface dominates over ΔT_{int} across the bottom interface, we do not know the spin mixing conductance for each interface and therefore we consider the effects of different interface terminations in Fig. S18. We assume that the AF domain is continuous in thickness, which is reasonable for 6-10 nm-thick NiO. The time-averaged sign of the ΔT_{int} is the same at both interfaces, and the sign of the spin current $\boldsymbol{J}_s$ must follow that of the thermal gradient in linear response. We show in Fig. S18 that $\boldsymbol{J}_c$ and therefore the AF LSSE voltage from each interface adds together when the top and bottom spins are parallel (a) and cancels out when they are antiparallel (b).

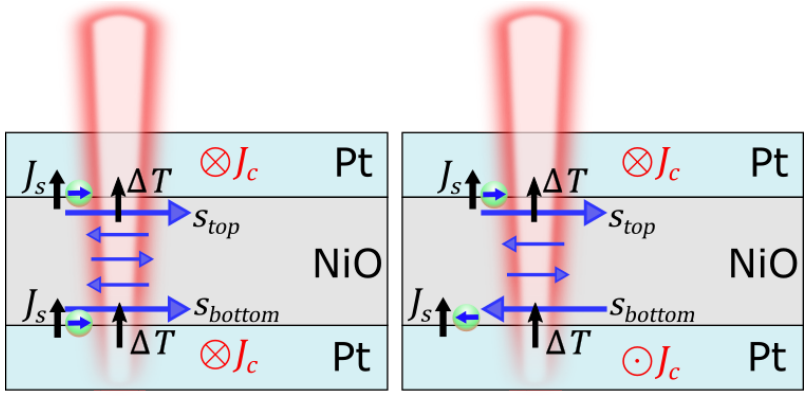

FIG. S18: Schematic showing the interfacial spin Seebeck voltage produced from two Pt/NiO interfaces. $\mathbf{J}_c$ adds together when the interfacial uncompensated spins are parallel (a) and cancels out when the spins are antiparallel (b).

This result would initially seem to hinder imaging of switching in trilayers, because only

regions with antiparallel top and bottom spins contribute to switching according to the argument of Refs. [3] and [15]. However, we argue AF LSSE imaging should still show switching, as follows: although we expect that spatial variation between parallel and antiparallel spins occurs on the nanometer scale, we also expect that the exchange coupling between spins causes domain rotation on the scale of hundreds of nanometers. Therefore the parallel regions that contribute to the AF LSSE signal are dragged along by the antiparallel regions that contribute to switching. The 650 nm laser spot size averages out surface roughness to yield a net signal that is proportional to N_x.

S9. AVERAGING PROCESS FOR AF LSSE IMAGES

In the main text, we compare images of the Néel orientation with the electrical readout by averaging the pixels in the AF LSSE images in and near the center of the 10 μm-wide Hall cross and comparing to R_H. As shown in Figure S19, we average pixels within a 12 μm-wide square centered on the cross center to ensure that contributions from the corners are incorporated. The correct dimensions that should be used for the averaging window are not obvious, since current flow is non-uniform within the cross. Therefore, the error bars on the average $V_{AF\ LSSE}$ in Fig. 3(e)in the main text are determined by calculating the change in the average $V_{AF\ LSSE}$ after varying the dimensions of the averaging window by 2 pixels in both the x and y-directions. In principle the pixels within the averaging window should also be weighted by the spatially-varying current density, but as a first approximation we average all pixels equally.

S10. ADDITIONAL IMAGES OF DOMAIN ROTATION AND DOMAIN WALL MOTION IN A Pt/NiO BILAYER

Fig. 4 in the main text shows domain rotation and domain wall motion in a MgO/Pt/NiO bilayer in response to current densities between 5.0×10^7 A/cm^2 (20 mA) and 1.1×10^8 A/cm^2 (42 mA). There we show images after +30 mA, +42 mA, -20 mA, and -42 mA. In Fig. S20 we show an expanded version of Fig. 4 with additional AF LSSE images after applying +20 mA and -42 mA. (Note the images were taken in order of ascending current density from +20 mA to +42 mA, then -20 mA to -42 mA.) We also show cumulative image differences

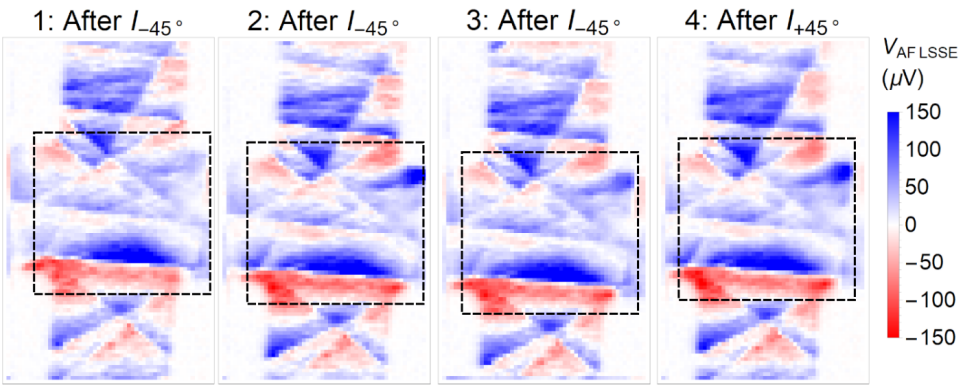

FIG. S19: The AF LSSE images from Figure 3 of the main text. We obtain the average $V_{AF\ LSSE}$ values in Fig. 3(c) and Fig. 3(e) by averaging all the pixels in each image within a 12 μm × 12 μm square region centered on the cross center, represented by the dashed lines.

in addition to the sequential image differences in Fig. 4(b).

Image *2* after +20 mA shows similar domain rotation and domain wall motion as image *3* after +30 mA, only weaker. The cumulative image differences in Fig. S20 show that after the domains in the bottom branch of the sample have rotated in *3*, their orientation remains largely fixed after further applications of current.

Lastly, to observe time-dependent effects of AF switching, we image after applying 1.0×10^7 A/cm^2, image again after 30 minutes, and take sequential and cumulative image differences in Fig. S21. This was done before taking the images in Fig. S20. We observe apparent domain rotation immediately after switching in $2 - 1$. $3 - 2$ shows domain wall motion after 30 minutes, even with no stimulus (also shown later in Section S8). The cumulative difference in $3 - 1$ resembles the differences in Fig. 4(b) in the main text, but fainter. We speculate that after the spin torque rotates the AF domains out of equilibrium, magnetoelastic stresses exert forces on the domain wall which result in subthreshold domain wall creep. As discussed in the main text, the switched states after +30 mA and +42 mA are stable in time, meaning they do not relax back, but the domain wall motion after +42 mA requires less current to reverse (at most -20 mA), which suggests that the switched state is metastable.

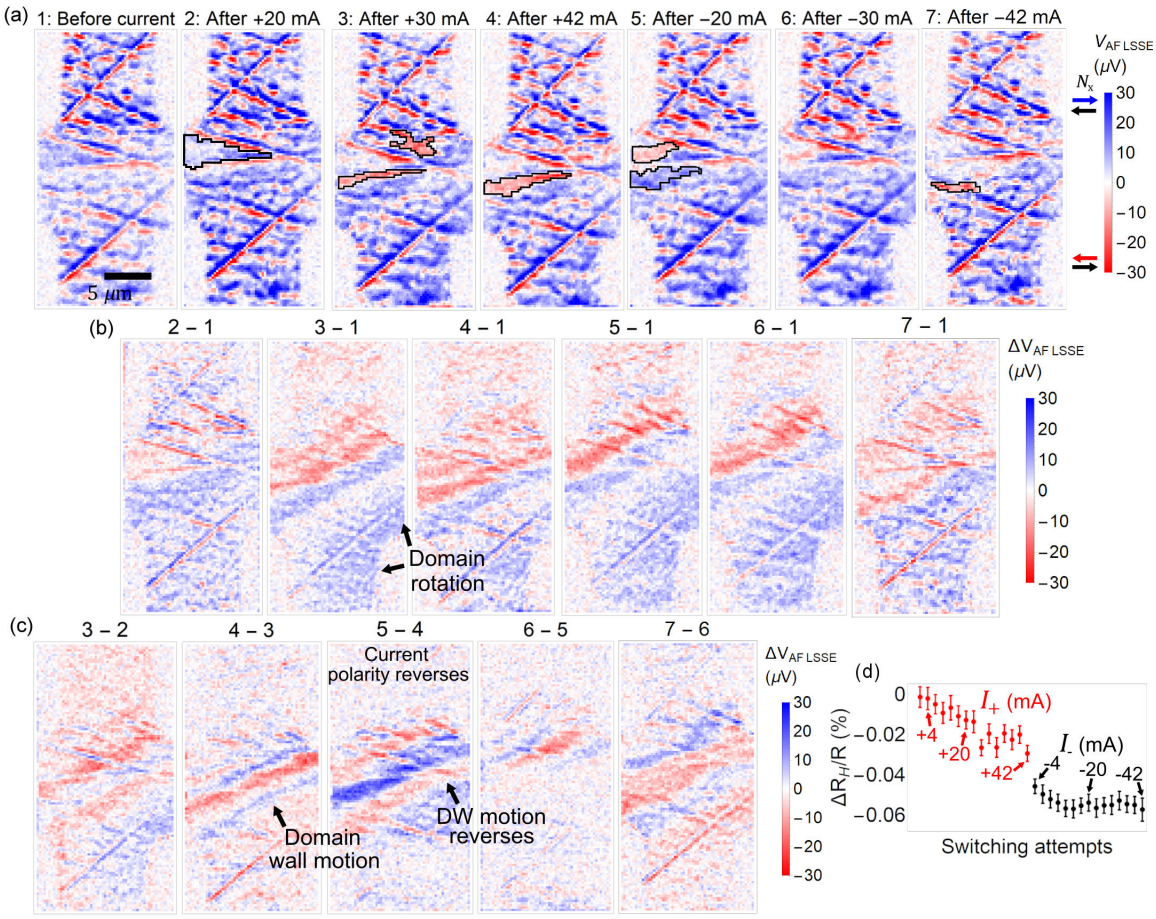

FIG. S20: Extended version of Fig. 4 from the main text. (a) AF LSSE images, including additional images after applying +20 mA and -42 mA. (b) Cumulative differences between the images in (a). Prominent domain rotation appears after +30 mA and remains after subsequent applications of current. (c) Sequential difference images as in Fig. 4(b). Weak domain wall motion appears after +20 mA.

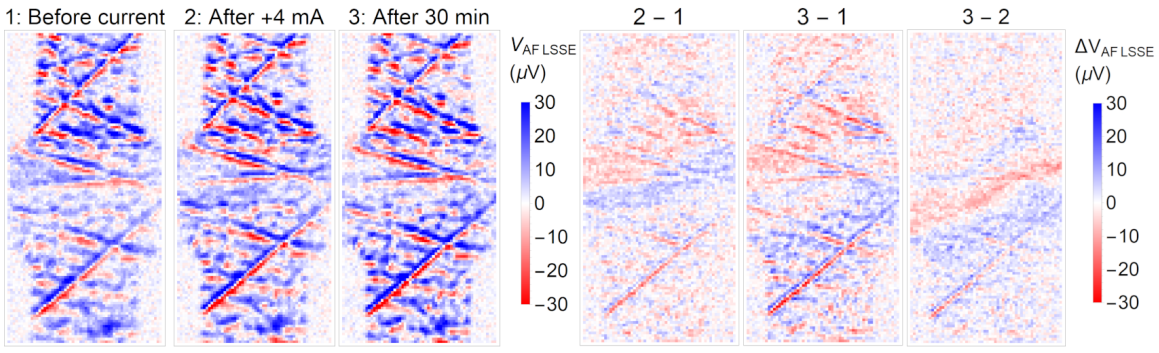

FIG. S21: AF LSSE images of the Pt/NiO bilayer from Fig. 4 in the main text before applying current, after applying 4 mA (1×10^7 A/cm^2), and after 30 minutes without stimulus. Initial domain rotation is followed by domain wall motion.

S11. CHARACTERIZATION OF SPIN-TORQUE SWITCHING

A. Experimental procedure for spin-torque switching and SMR reading

We use a Keithley 2400 sourcemeter for both spin-torque writing and electrical reading in all samples. The switching in Fig. 3 of the main text is done with DC current, applied for 5 s using a current density of 3.1×10^7 A/cm^2. Note that while applying current at $\pm 45°$ requires four electrical contacts, AF LSSE microscopy only works with two contacts: stray capacitance between four contacts at high frequencies causes signal leakage, making the images difficult to interpret. Therefore, we wire bond the two AF LSSE voltage contacts, and we perform spin-torque switching and SMR measurement using a probe station to make temporary contacts. In Fig. 4, where we apply writing current along the $V_{AF\ LSSE}$ voltage contacts, we do not have this difficulty. In the sample in Fig. 4, we apply writing current using a series of 10 2 ms-wide DC pulses.

B. SMR while toggling $I_{\pm 45°}$

To characterize both reproducibility of spin-torque switching at a given writing current density and the magnitude of switching as a function of current density, we measure R_H in an unannealed 15 μm-wide Hall cross after toggling between 45° and $-45°$ writing current directions as described in the main text. Results are shown in Fig. S22: each point represents R_H after toggling the current direction.

We find a much larger (100s of mΩ) change in R_H after the first several switching attempts at a given current density than the $\sim$50 mΩ changes that follow, which is consistent with a decrease in antiferromagnetic domain wall motion. Surprisingly, the polarity of switching seems to reverse, between $\boldsymbol{N}$ rotating towards $\boldsymbol{J}_W$ and $\boldsymbol{N}$ rotating perpendicular to $\boldsymbol{J}_W$, at 3.2×10^7A/cm^2, 3.9×10^7A/cm^2, and 4.2×10^7A/cm^2. This may be due to the chiral domain force $\boldsymbol{F}_{DW}$ documented by Ref. [11] and our work, which can result in both $\boldsymbol{N} \parallel \boldsymbol{J}_W$ and $\boldsymbol{N} \perp \boldsymbol{J}_W$, combined with different current thresholds for different regions of the sample. Further studies are necessary to determine long-term switching reproducibility in multidomain samples.

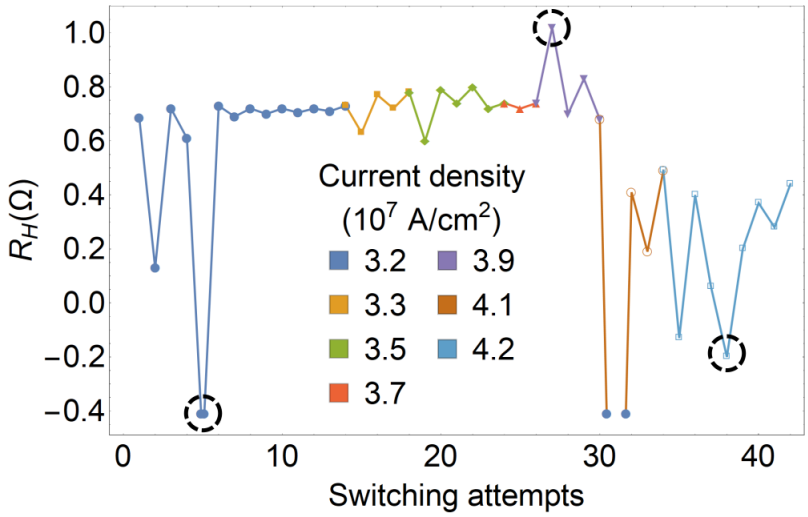

FIG. S22: R_H in a 15 μm-wide Pt/NiO/Pt cross as a function of writing current density, alternating between I_{45° and I_{-45° at each point. An initial ΔR_H of 100s of mΩ is consistently followed by $\sim$ 50mΩ changes, which may be correlated with the decrease in domain wall motion that we observe in LSSE images. At 3.2, 3.9, and 4.2 $\times 10^7$A/cm^2, highlighted in the plot, the polarity of the switching seems to reverse, which may be due to different threshold current densities for switching in different spatial regions of the sample.

S12. FINITE-ELEMENT SIMULATIONS OF CURRENT FLOW IN A CROSS

During the switching process, we apply current to adjacent arms of the cross such that the current flows along a 45° diagonal in the center, which means that the current density is spatially nonuniform. We simulate the spatial current profile in COMSOL in Fig. S23.

We estimate current densities of 3.8×10^7A/cm^2 within the channel, 3.1×10^7A/cm^2 at the center of the cross, and 8×10^7A/cm^2 at the corner. Higher current density at the corner is consistent with the switching profile in annealed NiO, shown in Figure 3 of the main text, where most of the repeatable switching occurs at the corner.

S13. COMMERCIAL DISCLAIMER

Certain commercial equipment is identified in this paper to foster understanding. Such identification does not imply recommendation or endorsement by NIST, nor does it imply

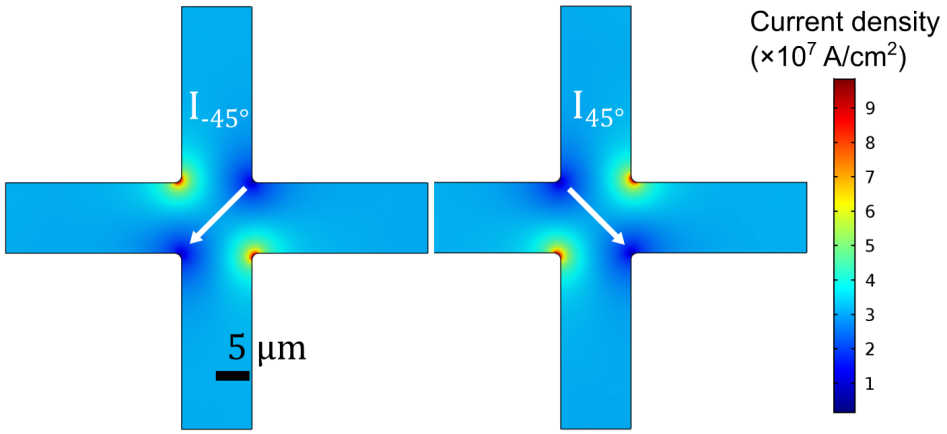

FIG. S23: Simulated magnitude of current density during the switching process, when the current is applied along a 45° diagonal. We estimate densities of $3.8 \times 10^7 \mathrm{A/cm^2}$ within the channel, $3.1 \times 10^7 \mathrm{A/cm^2}$ at the center of the cross, and $8.0 \times 10^7 \mathrm{A/cm^2}$ at the corner. This is consistent with switching occurring mostly at the sample corner in annealed samples, and also with switching occurring both within the cross channel and at the center in unannealed samples.

that the materials or equipment available are necessarily the best available for the purpose.

[S1] J. M. Bartell, D. H. Ngai, Z. Leng, and G. D. Fuchs, Nature Communications **6**, 8460 (2015).

[S2] J. M. Bartell, C. L. Jermain, S. V. Aradhya, J. T. Brangham, F. Yang, D. C. Ralph, and G. D. Fuchs, Phys. Rev. Applied **7**, 044004 (2017).

[S3] T. Moriyama, K. Oda, T. Ohkochi, M. Kimata, and T. Ono, Scientific Reports **8**, 14167 (2018).

[S4] I. K. Schuller, R. Morales, X. Batlle, U. Nowak, and G. Güntherodt, Journal of Magnetism and Magnetic Materials **416**, 2 (2016).

[S5] F. U. Hillebrecht, H. Ohldag, N. B. Weber, C. Bethke, U. Mick, M. Weiss, and J. Bahrdt, Phys. Rev. Lett. **86**, 3419 (2001).

[S6] F. L. A. Machado, P. R. T. Ribeiro, J. Holanda, R. L. Rodríguez-Suárez, A. Azevedo, and S. M. Rezende, Phys. Rev. B **95**, 104418 (2017).

[S7] S. Saito, M. Miura, and K. Kurosawa, Journal of Physics C: Solid State Physics **13**, 1513 (1980).

[S8] A. Y.-C. Yu, W. E. Spicer, and G. Hass, Physical Review **171**, 834 (1968).

[S9] R. Newman and R. M. Chrenko, Physical Review **114**, 1507 (1959).

[S10] R. M. Costescu, M. A. Wall, and D. G. Cahill, Phys. Rev. B **67**, 054302 (2003).

[S11] L. Baldrati, O. Gomonay, A. Ross, M. Filianina, R. Lebrun, R. Ramos, C. Leveille, T. Forrest, F. Maccherozzi, E. Saitoh, J. Sinova, and M. Kläui, arXiv e-prints , arXiv:1810.11326 (2018), arXiv:1810.11326 [cond-mat.mtrl-sci].

[S12] Y. Cheng, S. Yu, M. Zhu, J. Hwang, and F. Yang, arXiv e-prints , arXiv:1906.04694 (2019), arXiv:1906.04694 [cond-mat.mes-hall].

[S13] P. Zhang, J. Finley, T. Safi, and L. Liu, arXiv e-prints , arXiv:1907.00314 (2019), arXiv:1907.00314 [cond-mat.mes-hall].

[S14] M. Charilaou and F. Hellman, Journal of Applied Physics **117**, 083907 (2015).

[S15] T. Moriyama, W. Zhou, T. Seki, K. Takanashi, and T. Ono, Phys. Rev. Lett. **121**, 167202 (2018).